Assessment of RANS Turbulence Models for Strut-Wing Junctions

Kyle C. D. Knight

Thesis submitted to the Faculty of the

Virginia Polytechnic Institute and State University

in partial fulfillment of the requirements for the degree of

Masters of Science

in

Aerospace Engineering

Chris J. Roy, Chair

William H. Mason

Joseph A. Schetz

April 18, 2011

Blacksburg, Virginia

Keywords: Transonic, Turbulence, Interference

Assessment of Reynolds Averaged Navier Stokes Equations Turbulence Models for a Strut-Wing Junction

ABSTRACT

Kyle C. D. Knight

Multidisciplinary Design Optimization (MDO) studies show the Strut/Truss Braced Wing (SBW/TBW) concept has the potential to save a significant amount of fuel over conventional designs. For the SBW/TBW concept to achieve these reductions, the interference drag at the wing strut juncture must be small compared to other drag sources. Computational Fluid Dynamics (CFD) studies have concluded the interference drag is small enough for the TBW concept to be practical. However, the turbulence models used in these studies have not been validated for transonic, high Reynolds number, junction flows. This study intends to assess turbulence models by comparing drag and surface streamlines obtained from experiment and CFD. The test model is a NACA 0012 fin at Mach number of 0.75 and a Reynolds number of 6 million with varying angle of attack. The CFD analysis includes both the fin and tunnel test section. The main turbulence model tested is the k-ω Shear Stress Transport model. The fin is tested at different Mach numbers and inlet conditions to account for experimental variations. The study shows the CFD over predicts separation. The reasons for this discrepancy is likely the turbulence models employed.

Dedication

I would like to dedicate this work to my parents, Terry and Laura Knight, and my grandparents, Stuart and Carola Cohn. Their love and support over the years has made it possible for me to excel.

Acknowledgments

Contents

List of Figures

List of Tables

Chapter 1

Introduction

1.1 Motivation

Since recorded history humankind has searched for ways to travel farther and faster with less effort. From pack animals and domestication of horses to truck and trains, the quest culminated with airliners, which transport people and cargo miles above the earth for many hours near the sonic barrier. However, airliners incur significant costs such as consuming tons of fuel, generating pollution at high altitude, and producing noise at takeoff [1],[2]. It is an aircraft designers job to mitigate these costs.

The first jet airliner with the current configuration was introduced for passenger service in 1958 with the Boeing 707 aircraft, seen in Figure 1.1. Airliners fly at high altitude, above 25 kft, and speeds of approximately 600 mph (M = 0.85), placing them in the high Reynolds number transonic flow regime. Since the 1950s airliner efficiency has continually increased,

the pinnacle of which is widely regarded as the Boeing 787 "Dreamliner," also seen in Figure 1.1 [3].

Economically, increases in fuel cost cause demand for even more fuel efficient airplanes. NASA has introduced "N+3" targets, where N+3 stands for three generations of aircraft technology forward, to be reached by 2025. These targets include noise reduction at takeoff by 71 dB, lower emissions by 75%, and decreasing fuel burn by 70% [6],[7]. This means further advances must take place.

The basic configuration of transport aircraft - a fuselage as a long tube and large swept wings - has not changed significantly since their inception. To emphasize this, the aircraft seen in Figure 1.1 are built by three different companies in three different countries over the span of 55 years. Note their basic configurations remain the same. Designers are now considering changes to the configuration, a bold move as many aspects of current transport aircraft have been optimized for the current configuration.

Several leading configuration changes are being considered, including hybrid flying wings, non-body of revolution fuselages, and strut or truss braced wings (SBW/TBW); the latter is the focus of this thesis. The SBW/TBW was first proposed by Pfenninger in 1954 and did not see significant investigation until recently when configuration changes were seriously considered [8]. The TBW concept involves a high wing aircraft with struts or trusses to strengthen the wings. A comparison between a conventional airliner and TBW can be seen in Figure 1.2. The SBW/TBW offers the following advantages over conventional aircraft:
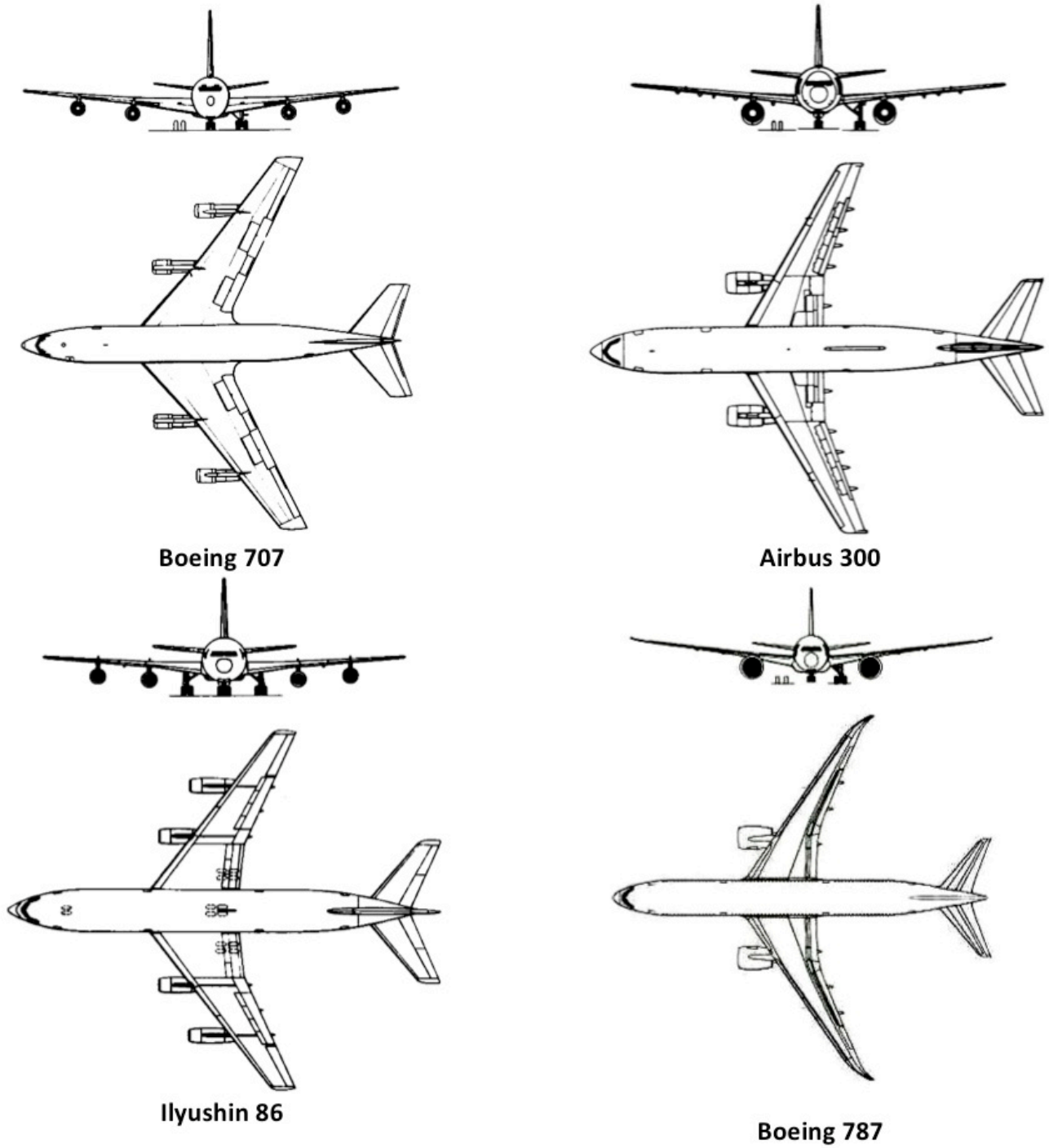
Figure 1.1: Top and front view of several airliners. (Note: aircraft are not to scale) [4],[5].
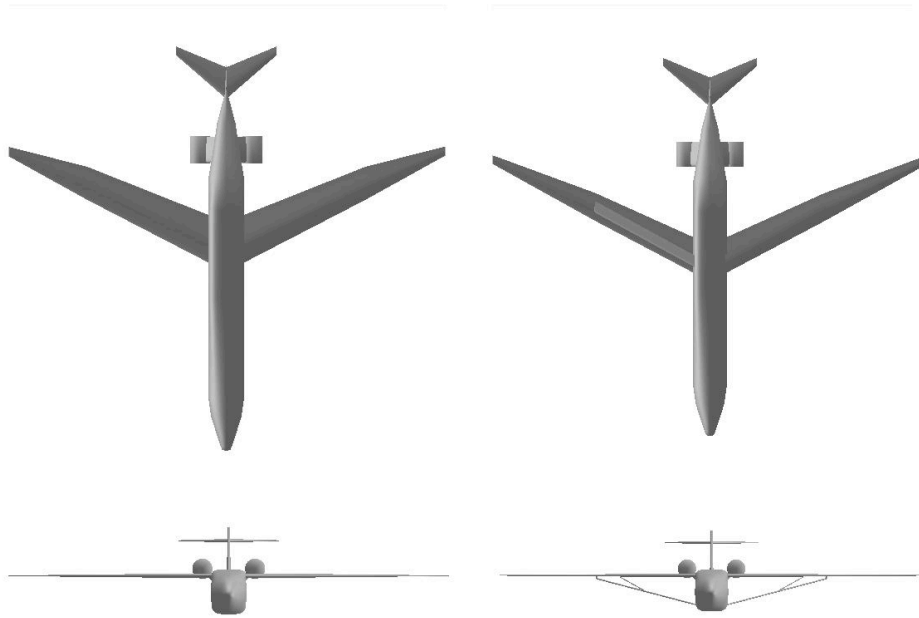
Figure 1.2: Left: Conventional airliner configuration top and front view. Right: TBW top and front view. Note longer, thinner wings on the TBW [9].

- Increased laminar flow over the wings

- Less weight due to reduced internal structure

- Reduce induced and wave drag due to higher spans and thinner wings

- Multidisciplinary Design Optimization (MDO) studies show 20% reduction in fuel consumption [1],[2]

The SBW/TBW configuration has several technical challenges to overcome before it becomes a viable design option. The top issues are intensive structural design of the wings, airfoil selection, and the interference drag at wing-strut and strut-strut junctures. The focus

of this thesis is interference drag prediction. Interference drag is the drag produced when two aerodynamic bodies intersect, which is generally larger than the drag produced by each separately. Previous computational predictions of interference drag have been performed, but little validation data exist for interference drag in high Reynolds number transonic flows [10],[11]. The interference drag predictions rely on the ability of the turbulence models to predict adverse pressure gradient induced separation. If interference drag predictions are incorrect, the simulation-based optimization of SBW/TBW concepts may not be possible. The purpose of this study is to assess turbulence models for interference drag predictions by comparing computational results with high Reynolds number transonic wind tunnel experiments.

1.2   Objectives and Scope

This project intends to evaluate the predictive capability of the one and two equation turbulence models to predict transonic interference drag. The models to be assessed are the Spalart-Allmaras, k-ω, and k-ω Shear Stress Transport (SST) turbulence models. These have been used in previous interference drag predictions [10],[11].

The predictive capability of selected turbulence models will be evaluated by performing a benchmark-level test. A benchmark test involves simplified physics and geometry of an experimental and computational model [12]. This benchmark test involves an unswept NACA 0012 wing attached perpendicular to a flat wall while angle of attack is varied.

The experimental portion is being performed in the transonic wind tunnel at the Univer-

sity of Texas at Arlington while the CFD portion is being performed at Virginia Tech. Both

CFD and experimental testing will measure streamlines near the airfoil surface along with

forces on the airfoil as the angle of attack is varied. To account for tunnel uncertainties the

CFD simulations will be run through a series of perturbations. The predictive capability of

the turbulence models will be assessed by comparing CFD simulations to experimental data.

1.3   Background

1.3.1   Transonic Flow

A fundamental flow property is the Mach number. Mach number is defined in equation

1.1 where M is the Mach number, V is the flow velocity magnitude, and a is the speed of

sound. The speed of sound is defined in equation 1.2 where γ is the ratio of specific heats, R

is the specific gas constant, and T is temperature. When a flow goes above $M = 1$ a shock, or

flow discontinuity, can form. Across a shock velocity decreases below $M = 1$, static pressure

increases, stagnation pressure decreases, and entropy goes up. Furthermore, shocks cause

wave drag. Together these are known as compressibility effects.

$$M = V/a \tag{1.1}$$

$$a = \sqrt{(\gamma R T)} \tag{1.2}$$

There are three major flow regimes defined by the Mach number: subsonic, transonic,
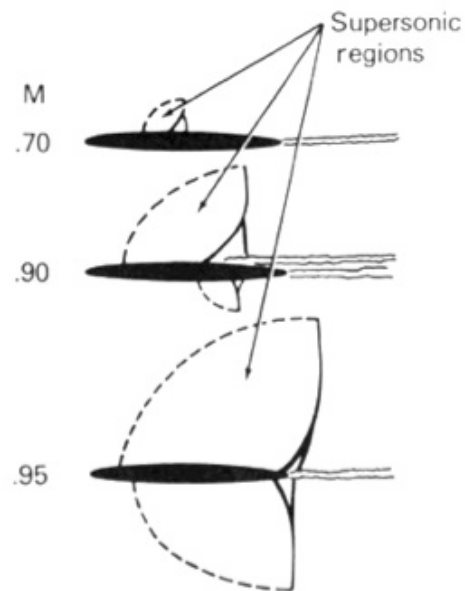
Figure 1.3: 2-D representation of transonic flows between $M = 0.70$ and $M = 0.95$ [13].

and supersonic. Compressibility effects are negligible in the subsonic regime, $M < 0.3$. Flow where the entire fluid is above $M = 1$ before a shock is called supersonic. Transonic flow is where the flow is locally supersonic across portions of a body and is typically defined between $M = 0.7$ and $M = 1.2$.

Most airliners fly between Mach 0.80-0.85, so it is critical to understand and predict transonic flow. A two dimensional representation of transonic flow is seen in Figure 1.3. These flows are even more complicated in three dimensions where the flow can be locally supersonic in three dimensions. These shocks increase wave drag and decrease efficiency. Predicting their effects is difficult because they are very sensitive to changes or uncertainties in Mach number, Reynolds number, and flow direction.

1.3.2   High Reynolds Number Transonic Flow

Reynolds number is a fundamental flow property defined as the ratio of viscous forces to inertial forces of a fluid. It is defined by equation 1.3 where ρ is the density, V is the velocity magnitude, L is a characteristic length, and μ is the dynamic viscosity. The flow properties ρ, V, μ are taken as the freestream values of the fluid. The characteristic length is typically the mean length of the object of study perpendicular to the flow. For most aerospace applications this is the chord of a wing.

$$Re = \frac{\rho V L}{\mu} \tag{1.3}$$

The MDO studies involve an aircraft flying at 40 kft at $M = 0.85$ with a strut that is 1-2 meters (3.28-6.56 feet) in length [1],[2]. The Reynolds number for this case is 7-9 million.

Reynolds (Re) number has a large influence on the location and effect of the shock. Early transonic wind tunnels operated at low Re number, 3 million or below [13]. When compared with flight test data, as seen in Figure 1.4, there is a large difference in the separated flow region.

In the late 1960s and early 1970s this problem was addressed by NASA and AGARD with a series of prototype test facilities using both pressure and cryogenic methods [14]. These facilities produced high Reynolds number flow in the transonic regime. This allowed the laboratory study of flow virtually identical to cruise speeds of modern aircraft. The prototype facilities led to two large scale high Reynolds number transonic facilities, the National Transonic Facility (NTF) in the US and the European Transonic Windtunnel (ETW) in Europe.

LOW REYNOLDS NUMBER

SHOCK

HIGH REYNOLDS NUMBER

SHOCK
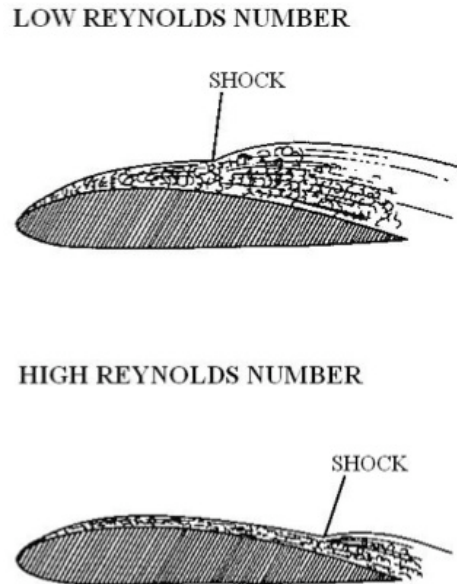
Figure 1.4: Illustration of the change in separation as Reynolds number increases [14].

While they provide a much better domain for experimental testing, they are expensive to operate and scheduling tunnel time is difficult. Therefore testing at this specific flow regime is limited because of the rarity and/or expense of tunnel time.

Shock induced separation typically occurs when $M_{local} > 1.3$ [15]. The shock interacts with the boundary layer, detaching the flow from the airfoil surface. The separated flow causes an increase in pressure drag, further reducing efficiency. Current turbulence models have a difficult time predicting separation size and location. Therefore these effects are difficult to predict computationally.

1.3.3 Prediction Methods

There are three methods used to predict the shock locations and their effects: flight tests, wind tunnel tests, and CFD analysis. Flight tests use a full scale flight vehicle or a scale model of the design construct. The flight vehicle is then flown at the desired conditions. These tests provide the best flow quality and a real world assessment of the problem. Mach and Reynolds number are tested near the design point. However, flight test models are very expensive, difficult to manufacture, and do not allow detailed study of the flow.

Wind tunnel tests use a model placed in a test section with desired flow conditions. If the purpose of the experiment is to explore a physical phenomena, the model is specially designed to assess this phenomena. If the experiment is closer to a flight test then a scale version of the actual component is used. Wind tunnel tests provide real world physics in a laboratory setting that allows measurement of additional flow properties. Reynolds number is generally lower than a flight test. Flow quality is lower than a flight test and facility dependent.

CFD analysis uses physics based models to solve the Navier-Stokes equations and computationally solve the flow for a given domain. CFD analysis is generally cheap to perform, flow properties are easy to assess, and perturbations, such as changes in flow speed and angle of attack, can be made quickly. CFD does not always capture all of the flow physics due to sub-models, discretization, and boundary conditions. Thus, important flow features may not be present or predicted correctly.

1.4 Interference Drag

1.4.1 Phenomena

Hoerner says interference drag occurs when "Two bodies ... touch or penetrate each other, ... when two or more bodies are placed one behind the other, or when two bodies are near each other (without really touching each other) [16]." Interference drag is defined as the drag that occurs when the bodies are in close proximity minus the drag produced by the two bodies on their own. This can be seen in equation 1.4, where D_{int} is the interference drag, $D_{together}$ is when the bodies are in close proximity, and $D_{individual}$ is the drag separately. Interference drag is often seen at strut-wing junctures, wing-body junctures, and engine pylons.

$$D_{int} = D_{together} - D_{individual} \tag{1.4}$$

1.4.2 Previous Research

Although interference drag has been a problem for a long time, prediction of strut effects at transonic speeds has been limited. Available data of interference drag for struts is restricted to low speeds and large thicknesses [16]. Engine pylon drag interference studies, which used CFD to lead experiments, were performed in the late 1980s and early 1990s, resulting in a new generation of low drag pylons called compression pylons. The studies demonstrate how CFD can be used to aid the design processes [17],[18],[19].

Strut-strut and strut-wing interference drag has been studied using CFD only. A study in 2000 at Virginia Tech by Tetrault, et al was used to create a response surface for MDO studies [10]. This work showed a large drag rise when the angle between the strut and wing was less than 45 degrees. This required a vertical offset of struts in MDO studies. A follow up study by Duggirala, et al in 2009 expanded on this work showing a slight decrease in interference drag at angles less than perpendicular [11]. This work also included better solution verification by using few unstructured cells, though more cells were used overall because of increases in available computing power.

CFD does not always include all of the relevant physics. Both Tetrault's and Duggirala's studies used the Spalart-Allmaras turbulence model, which has not been validated for high Reynolds number transonic strut interference flows. The accuracy of drag calculations is dependent on turbulence being correctly modeled.

1.5   CFD

The CFD code ANSYS Fluent 12.0 (Fluent) is used throughout industry and is a standard CFD solver at Virginia Tech. Fluent uses the Navier-Stokes equations (N-S) to compute three-dimensional (3-D), compressible, viscous fluid flows [20]. The Navier-Stokes equations are non-linear coupled partial differential equations (PDE) for which there are few known general analytical solutions [21]. The CFD problem may be simplified by reducing dimensionality and using simplifying assumptions such as steady, incompressible, and inviscid flow. Some of these features were used in preliminary tests, but for our purposes the 3-D steady

flow was calculated. Steady flow is calculated using the Reynolds Averaged Navier-Stokes (RANS) equations, which are computationally inexpensive compared to solving the unsteady flow via Large Eddy Simulation (LES) or Detached Eddy Simulation (DES). Three dimensions are required because strut-wall interference drag is an inherently 3-D problem.

Further detail on the governing equations, turbulence models, and discretization can be seen in Chapter 4.

1.6   Verification

Verification answers the question "are we solving the equations correctly?[12]" For almost all real world scientific computing cases exact solutions are not known beforehand. Therefore, the accuracy of any numerical results rely on the code solving the equations correctly. There are two types of verification, code and solution verification. The goal of code verification is to identify any coding errors. The goal of solution verification is to quantify numerical errors. More detail of verification and its implementation in this study can be seen in Chapter 5.

1.7   Validation

1.7.1   Introduction to Validation

Validation is the assessment of a sub-model in scientific computing. The two major types of validation are scientific validation and full system validation. Scientific validation usually inspects a physical phenomena using simplified physics in a laboratory setting. Full system

validation incorporates many coupled physical systems in a complicated physical system. This study is a type of scientific validation known as a benchmark test which involves a few coupled physical processes and a simplified system. For true benchmark tests, the boundary conditions and System Response Quantities (SRQs) are measured along with their associated uncertainties. The tunnel test section used in this study had several boundary conditions that could not be well characterized along with only a few measurable SRQs due to physical and resource limitations.

1.7.2   Validation Process

A validation experiment is a joint operation between experimentalists and computational analysts [12]. The computational analyst requests certain SRQs along with boundary condition measurements. Information about the associated uncertainties and limitations of both computation and experiments is exchanged between the two sides. As the series of experiments is performed, the experimentalists report the boundary conditions and some necessary flow quantities to the computational analyst; however, the SRQs should not be exchanged. The knowledge of the final SRQs could lead either the experimentalist or the computational analyst to change their processes, even unintentionally, to match the SRQ received from their counterpart.

After the series of experiments is performed the uncertainties associated with the measured quantities, except the SRQs, are sent to the computational analyst. These uncertainties are introduced to the simulation by slightly changing the boundary conditions or geometry.

The computational model is then run using a random selection of these uncertainties for many cases. The result is not a single number for the SRQs, but rather an interval for which they could exist. This statistical approach yields much more information to a decision maker.

1.8 University of Texas at Arlington Transonic Tunnel

The University of Texas at Arlington (UTA) transonic tunnel is a Ludwieg Tunnel. The tunnel is a special type of blowdown tunnel first proposed by its namesake, Hubert Ludwieg, in 1957 [22]. During a test, flow properties such as static pressure, stagnation pressure, and static temperature are measured. The test article is a NACA 0012 fin (Aspect Ratio = 2). It is equipped with a force and moment balance to measure drag. Visualization of the surface flow can be performed using oil dots. Dye is added to the oil to gain more information about the flow. The oil movement represents streamlines at the surface. More detail on the operation, geometry, and simplifications for CFD application can be found in Chapter 3.

Chapter 2

Literature Review

2.1 Interference Effects

2.1.1 Subsonic Calculations

Hoerner (1965) defines of interference drag and includes calculations based on experimental data [16]. Though a good interference drag resource for low speed flows and thick airfoils, the material cannot be extrapolated to transonic flow with thinner airfoils.

2.1.2 Compression Pylons

The development of compression pylons in 1982 provides an example where CFD led experimental development in transonic interference drag [17], [18], [19]. The studies show how designs were developed using Euler CFD codes which neglect viscous effects. The designs were then manufactured as scale models, analyzed experimentally, and modified to produce

the best performance.

2.1.3   Third AIAA Drag Prediction Workshop

The third AIAA drag prediction workshop involved a European designed model that was analyzed experimentally along with CFD [23]. The experimental portion of the test was performed at NASA Langley and ONERA facilities. The CFD portion was performed by several research groups and companies using several different grids. The test conditions were at a Reynolds number of 3 and 5 million an ranged from a Mach number of 0.4 to 0.8. The interference effects were in a wing-body junction. A separation bubble was present in both experiments and with CFD analysis, though CFD analysis disagreed on the size of the bubble. The workshop reached many conclusions. The most relevant is the separation zone behavior changed depending on turbulence model, grid family, and grid type. The two main turbulence models employed were the Spalart-Allmaras and the k-ω SST models. The k-ω SST model predicted higher total drag, higher pressure drag, and lower skin friction drag than the Spalart-Allmaras model. This was true across various solvers and grid types.

2.2   Experimental Data for NACA 0012

The Advanced Technology Airfoil Test (ATAT) program developed a large portion of the data for high Reynolds number transonic testing [24]. The ATAT tested airfoil technology at Mach numbers from 0.3 to 0.82 and Reynolds numbers from 3.0 million to 45.0 million. The tests examined the nominal 2-D performance of the airfoils by placing them across the

span of a wind tunnel perpendicular to the tunnel walls. The program tested NACA and industry airfoils at NASA Langley's 0.3-meter cryogenic tunnel [25]. To check for tunnel effects, some of the airfoils were tested at NASA Langley's 8-foot transonic tunnel and the DFVLR transonic facility in Germany [26], [27].

The NACA 0012 is a popular airfoil in subsonic and transonic research since it is a well characterized airfoil. For this reason, the NACA 0012 airfoil was tested in both NASA Langley's 8-foot transonic tunnel and 0.3-meter cryogenic transonic tunnel [26],[24]. The 0.3-meter tunnel test obtained pressure data at the center of the span, across the span, and close to the wall. Data was not collected close enough to the side wall to detect interference effects, so it could not be used in this study. Other airfoils tested in the 0.3-meter tunnel included Boeing's BAC I and TR77 along with some European airfoils [28],[29],[27].

As part of the ATAT studies side wall boundary layer effects were investigated. The boundary layer was studied with and without suction upstream of the airfoil location [30]. Suction was used to reduce the effects of the boundary layer on the airfoil. Another study highlighted wall interference along with a correction procedure [31]. Since only the two dimensional performance of the airfoils was required, interference effects were seen as a nuisance for these tests. Therefore, there is very little practical data for these effects.

2.3   Turbulence Models

2.3.1   Shock Induced Separation

Turbulence models ability to predict shock separation has seen varied success. For mild pressure gradients and little to no separation, the Baldwin-Lomax model compares well with experimental data [32],[33]. A study compares Wilcox's multiscale and k-ω models to experiment for shock induced separation. Both models predict separation similar to experimental values with the multiscale model predicting separation better [34],[33].

2.3.2   Adverse Pressure Gradient

Both Menter and Wilcox discuss the modeling of adverse pressure gradient flows using turbulence models [35],[33]. The consensus is that the k-ϵ model does not compare well with experimental adverse pressure gradient data while the k-ω and k-ω SST models compare well with this data. The experimetal data includes several different types of flows and flow regimes. Menter makes the case that k-ω SST provides the best comparison with experimental data of the turbulence models mentioned.

2.3.3   Thick Airfoils with a Flat Wall Juncture

A study by the Australian Defence Science and Technology Organisation (DSTO) compares experimental data to CFD results for a thick airfoil attached to a flat wall at low Mach and Reynolds number [36]. Though the flow regime is much different, the geometry is very

close to that used in this study. Furthermore, the flow is subject to a tunnel wall boundary layer. The CFD analysis used the same CFD code as the current study, Fluent. The study compared various turbulence models, and determined the k-ϵ model did not compare well with the data while the V2F model produced the best comparison [35],[20]. The Reynolds Stress Model, Spalart-Allmaras, and k-ω models were also tested [37],[33],[20]. Compared to the experimental data these models produced similar levels of accuracy, which was between the k-ϵ and V2F models.

2.4   CFD Applied to SBW/TBW

Work at Virginia Tech in 2000 involved the calculation of interference drag for a flight vehicle concept along with an analysis at wing-strut junctures [10],[38]. The latter study involved simulating the wing-strut juncture while varying the angle between the strut and the wing. The study concluded minimum drag occurs when the strut is perpendicular to the wing.

Further work at Virginia Tech in 2010 expanded the previous studies by performing a similar study with more angles between the strut and the wing [11]. The grids were improved by using a more refined, fully structured grid. This was possible due to increases in computational power. The study concluded angles below perpendicular could produce lower interference drag than perviously thought. The main turbulence model employed was the Spalart-Allmaras model. The k-ω model was also used and showed good agreement with the Spalart-Allmaras model.

Station	Calculation	Experiment
y = 2 mm (η = 0.6%)	0.6974	0.6651
y = 10 mm (η = 2.9%)	0.7074	0.6830
y = 20 mm (η = 5.9%)	0.7186	0.6885
y = 40 mm (η = 11.8%)	0.7298	0.7127
y = 80 mm (η = 23.5%)	0.7346	0.7186
y = 170 mm (η = 50.0%)	0.7382	0.7205

Figure 2.1: Coefficient of normal force (C_n) at spanwise locations.

Both CFD studies used data from Bartelheimer, et al. to perform validation studies of transonic junction flows [39]. The configuration is a wing across a test section at $M = 0.73$ and a Reynolds number of 6 million. The first study by Tetrault et al. showed some discrepancies between the experimental and CFD normal force data as seen in Figure 2.1. However, the CFD data is close to experiment and follows the same trend. The later study by Duggirala, et al. compared pressure coefficient plots at several spanwise locations. These data can be seen in Figure 2.2 show much better agreement, though some pressure points are outside of experimental values.
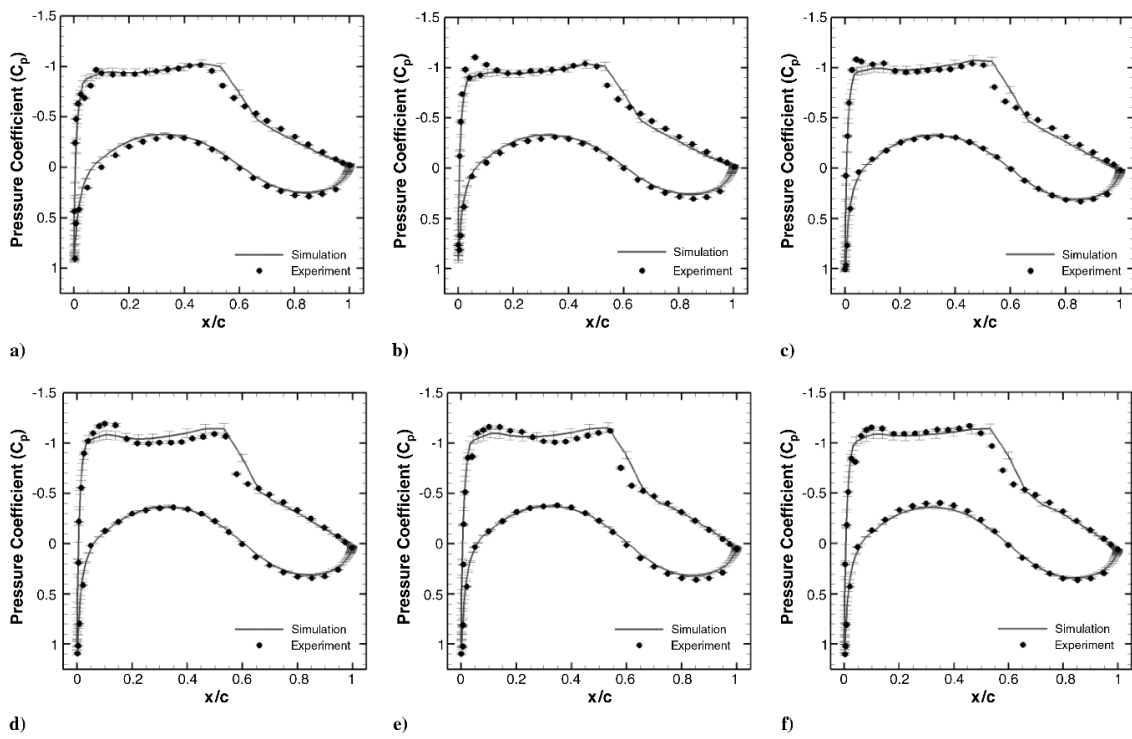
Figure 2.2: Pressure coefficient plots at several spanwise locations.

Chapter 3

UTA Tunnel

The system of interest is the University of Texas at Arlington (UTA) transonic wind tunnel. The apparatus is a special type of expansion tube called a Ludwieg tunnel. Figure 3.1 shows the specific Ludwieg tunnel used in this study [40]. The tunnel is unique because it operates at high Reynolds numbers in the transonic regime, $0.6 < M < 1.2$. The tunnel was originally operated at Arnold Engineering Development Center (AEDC), but has since moved to UTA.

3.1 Operation

The tunnel operates by pressurizing the charge tube, converging nozzle, and test section (see Figure 3.1) to attain the correct Mach and Reynolds number. The operation of the tunnel is characterized in Chapter 1. Ludwieg tunnels generally operate at high Mach number, but the UTA Ludwieg tunnel is unique because it operates in the transonic regime.
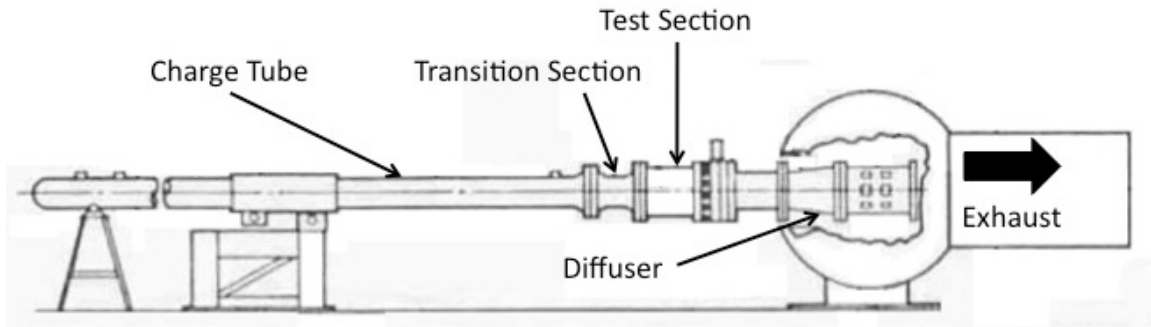
Figure 3.1: Full view of the AEDC Ludwieg Tunnel now used at UTA [40].

If the walls are solid, like most wind tunnels, a shock chokes the test section. The UTA tunnel allows shocks to dissipate via porous walls on the top and bottom. The side walls remain solid. The back pressure of the porous walls is adjusted to attain the desired Mach number in the tunnel section. The total tunnel porosity is approximately 5.5% [41]. The tunnel operates at atmospheric temperatures and stagnation pressures of 345 kPA to 3.45 kPa. The Reynolds number ranges from 2 to 20 million for a chord length of 0.0508 m (2 inches).

3.2 Modeling the Test Section

3.2.1 Simplifications

The charge tube, transition section, and valve opening would have to be modeled to fully simulate the UTA tunnel. This is not feasible for a few reasons. Modeling the entire tunnel would require large computational and time resources. The as-built geometry of the charge tube and especially the transition section would be required; they are currently unavailable.
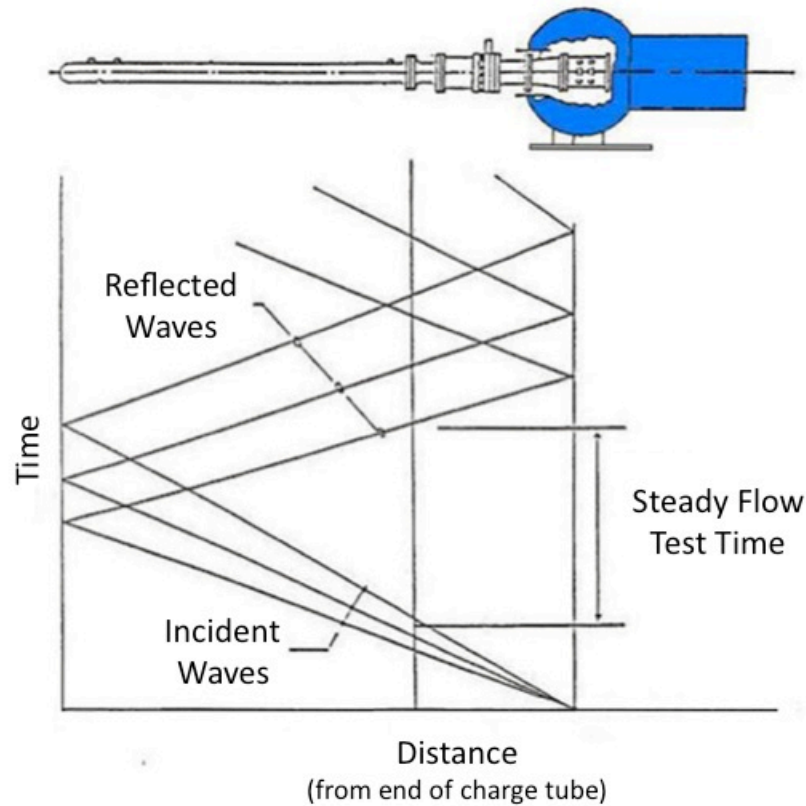
Figure 3.2: x-t diagram of the UTA Ludwieg Tunnel.

Finally, this study is only interested in the flow at and around the NACA 0012 fin. Since it is infeasible to model the entire tunnel and only the region near the airfoil is important for our study, only the test section is modeled.

The physics must be simplified along with the geometry. The shock tube process produces an unsteady wave, but this study assumes steady state and only models the tunnel start and ending conditions. Tunnel Mach and Reynolds number are relatively constant through the run. Only the test section entrance boundary layer changes significantly. The entrance boundary layer is determined from prior experimental measurements.

Experimental tests show transition occurs very close to the stagnation point at the leading edge. Because of this, there is no trip strip on the NACA 0012 fin and the CFD model assumes fully turbulent flow for the NACA 0012 model.

3.2.2   Test Section Model Geometry

The test section has a rectangular cross-section and is 64.45 cm (25.375 inches) long, 18.6 cm (7.332 inches) tall and 23.25 cm (9.15 inches) wide. A side view can be seen in Figure 3.3 The test model is a NACA 0012 unswept fin with a chord of 2 inches and a span of 4 inches (see Figure 3.4). The tip of the fin is rounded by rotating the airfoil geometry about the chord. The base of the fin is flush against the test section side wall. The set up allows angles of attack from -5 to +5 degrees.

3.2.3   Simulation of the Boundary Layer

The desired test conditions are achieved in the test section after the expansion wave crosses the transition section and before it is reflected and crosses again. During this time the fluid reaching the test section has traveled the length of the charge tube. This means the tunnel wall boundary layer grows as the test proceeds.

Inlet boundary layer data were obtained from the wind tunnel when it was still located at AEDC. The data were obtained at M=0.85 and Re=5E6 and can be seen in Figure 3.5 [43]. The AEDC boundary layer data were curve fitted and put into a useable form for the tunnel start and finish conditions. The data were measured at the inlet as seen in Figure

3.6. This curve fit was then applied as a stagnation pressure distribution at the inflow plane. The boundary layer is assumed to grow such that the boundary layer height, $\delta_{U_e=0.99}$, matches across the inlet and in the corners. A visual representation is seen in Figure 3.7. The simulation is then run at the start and finish conditions to gain a perspective on how the results change with boundary layer growth.

3.2.4 Assumptions

Validating CFD models requires well defined boundary conditions. Poorly defined boundary conditions specific to the UTA Tunnel are the porous walls and the entrance boundary layer. CFD models for the porous wall boundary conditions introduce large uncertainties. For this study, solid walls are assumed.

There are little experimental data for the tunnel entrance boundary layer. Boundary layer growth is assumed to be uniform across the test section. Figure 3.7 shows how the boundary conditions are applied. The experimental conditions where the entrance boundary layer was measured are close enough to our conditions to assume the same boundary layer behavior. Experimental data at the entrance measures $\delta_{80\,ms} = 1$" at 80 ms. The boundary layer profile is shown in Figure 3.5. Assuming the tunnel runs for 100 ms, the finish condition for the boundary layer is interpolated to be $\delta_{180\,ms} = 2$". Ultimately, the porous wall and entrance boundary conditions can only be estimated. This is an unknown until further experimental data are obtained.

TOP POROUS WALL

0.03125 GAP BETWEEN MOUNT AND WALL

7.332

3.666

BOTTOM POROUS WALL

16.355 TO 1/4 CHORD
15.855 TO FRONT TIP

25.375
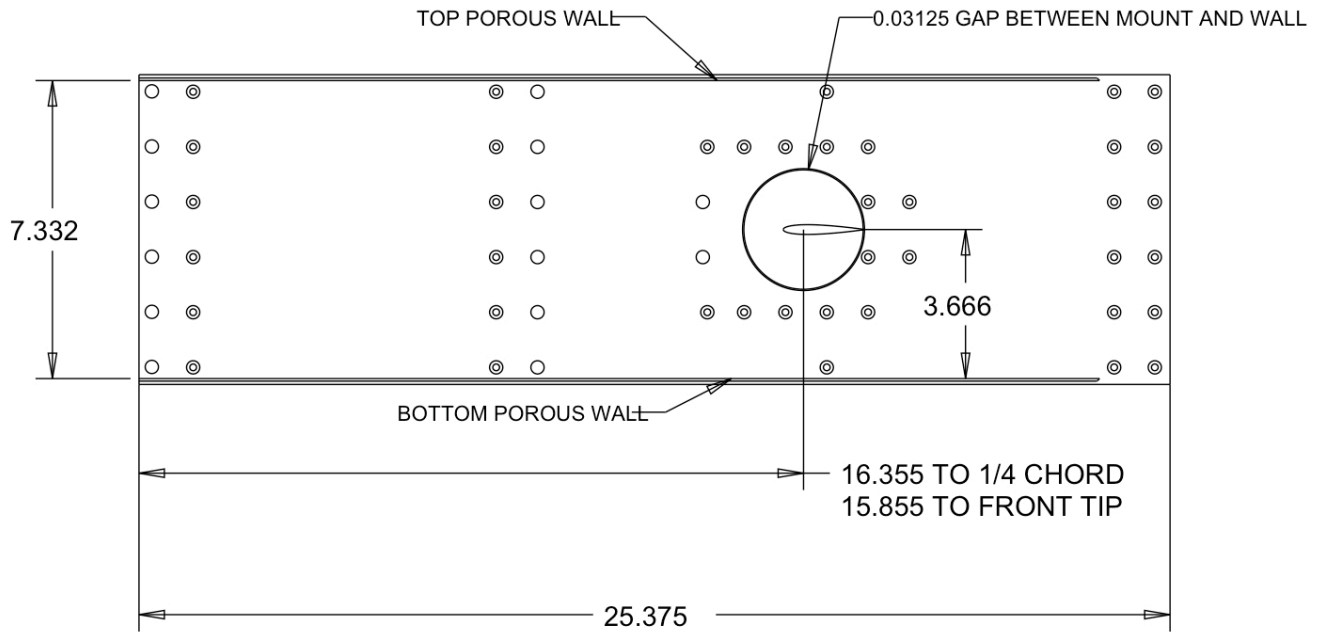
Figure 3.3: Technical drawing of the UTA test section side wall in inches [42].
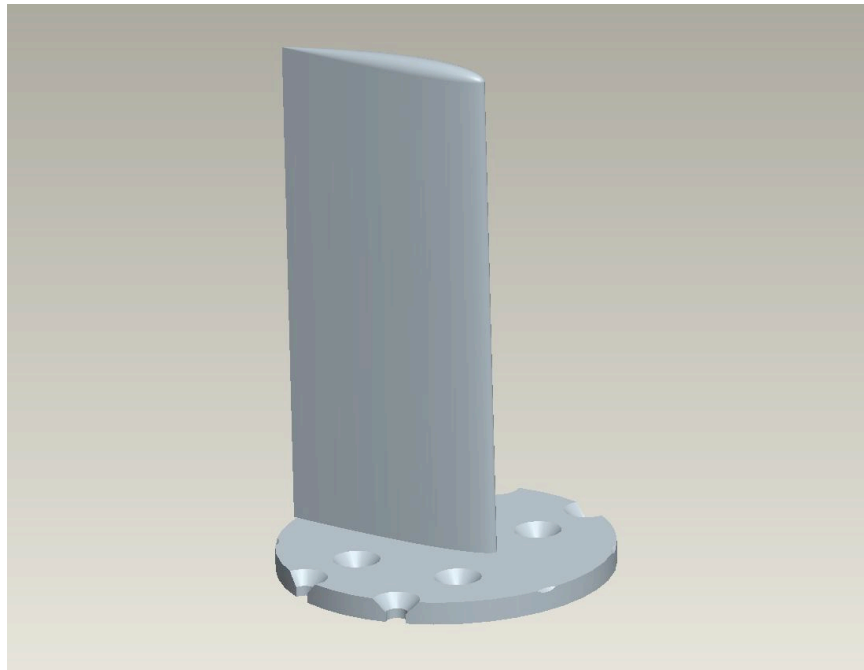
Figure 3.4: CAD drawing of the NACA 0012 fin to be placed in the UTA tunnel.
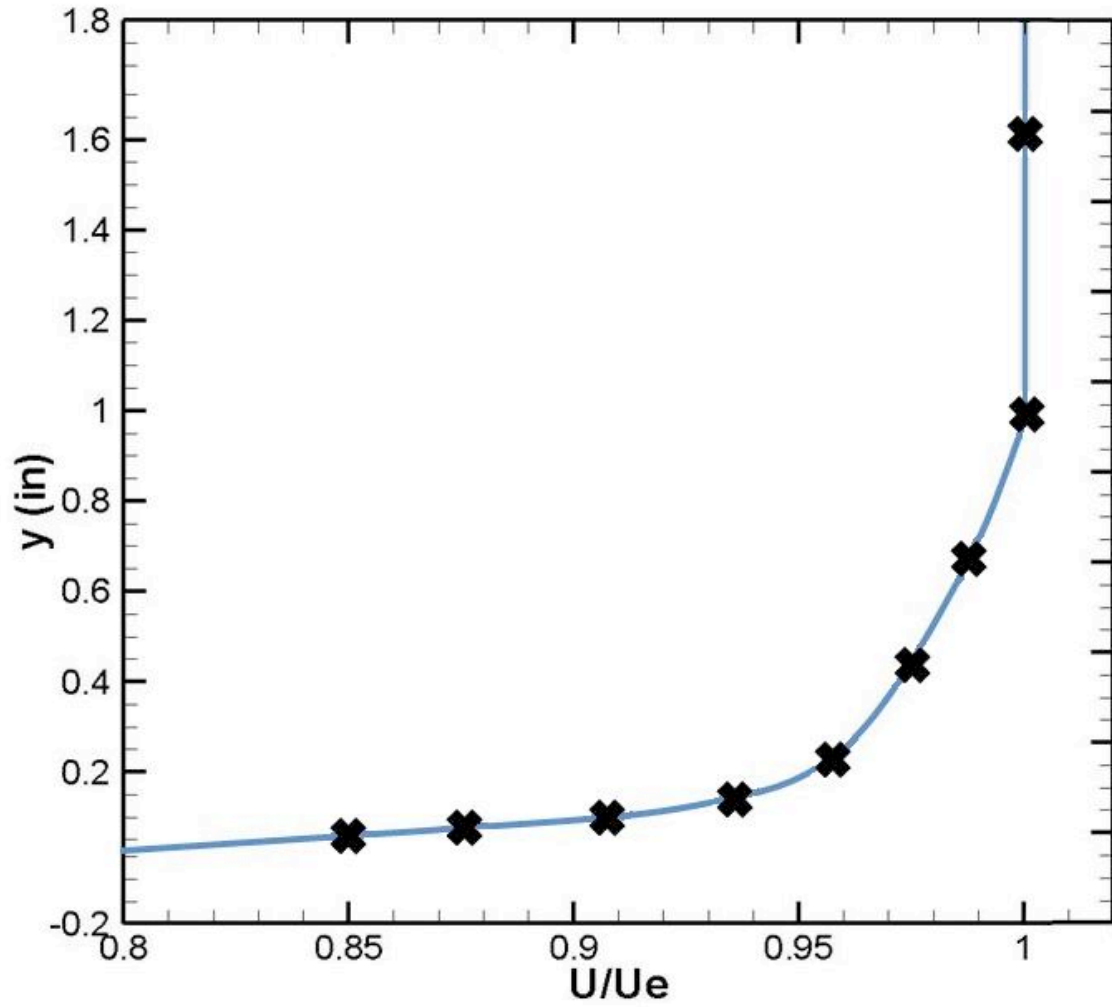
Figure 3.5: Boundary layer profile from AEDC data at tunnel start conditions.
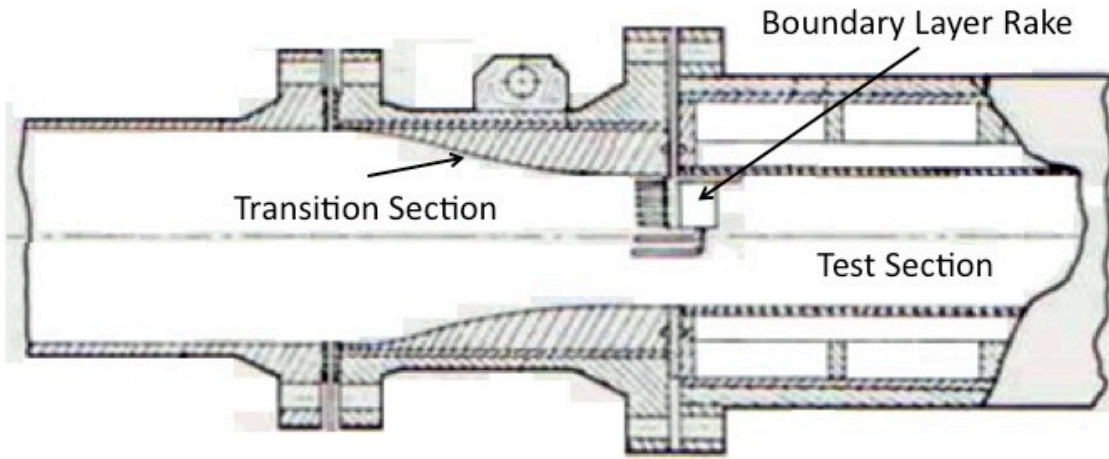
Figure 3.6: UTA Ludwieg tunnel test section with boundary layer rake.

$$\delta_{\frac{U}{U_e}=0.99} = 5.08 \; cm = 2.00 \; inches$$

$$\delta_{\frac{U}{U_e}=0.99} = 2.54 \; cm = 1.00 \; inches$$
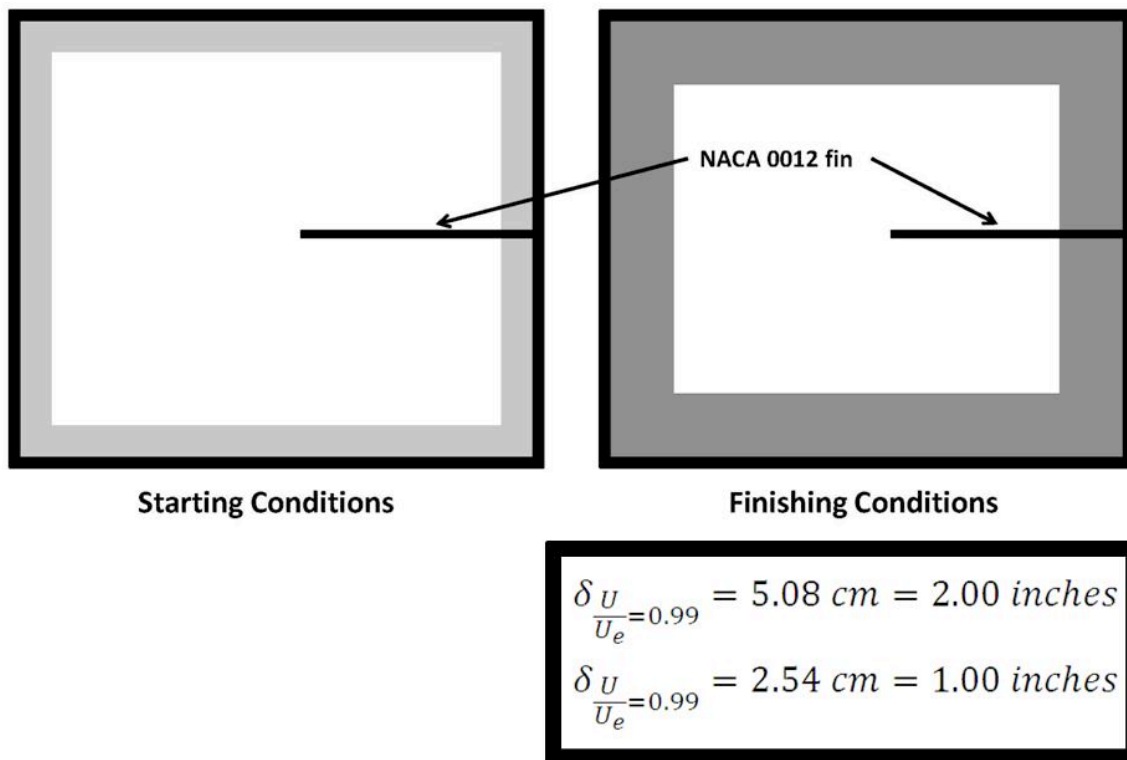
Figure 3.7: Boundary layer representation as seen from behind the NACA 0012 fin.

Chapter 4

Governing Equations and

Discretization

4.1 RANS

The governing equations are modeled using the steady 3D, Favre averaged, Navier-Stokes (RANS) equations, 4.1 - 4.5. The laminar stress tensor (t_{ij}), turbulent stress tensor (τ_{ij}), and turbulent and laminar heat flux terms are given by equations 4.6, 4.7, and 4.8, respectively. The equation of state, total energy, e_t, and the total enthalpy, h_t, are given in equations 4.9, 4.10 and 4.11, respectively. A note on notation, the overbar, $\bar{\rho}$ indicates time averaging while the tilde, $\tilde{u}$, indicates mass averaging.

$$\frac{\partial(\bar{\rho}\tilde{u})}{\partial x} + \frac{\partial(\bar{\rho}\tilde{v})}{\partial y} + \frac{\partial(\bar{\rho}\tilde{w})}{\partial z} = 0 \tag{4.1}$$

$$\frac{\partial(\bar{\rho}\tilde{u}^2 + p - \bar{t}_{xx} - \tau_{xx})}{\partial x} + \frac{\partial(\bar{\rho}\tilde{u}\tilde{v} - \bar{t}_{xy} - \tau_{xy})}{\partial y} + \frac{\partial(\bar{\rho}\tilde{u}\tilde{w} - \bar{t}_{xz} - \tau_{xz})}{\partial z} = 0 \qquad (4.2)$$

$$\frac{\partial(\bar{\rho}\tilde{v}\tilde{u} - \bar{t}_{xy} - \tau_{xy})}{\partial x} + \frac{\partial(\bar{\rho}\tilde{v}^2 + p - \bar{t}_{yy} - \tau_{yy})}{\partial y} + \frac{\partial(\bar{\rho}\tilde{v}\tilde{w} - \bar{t}_{xz} - \tau_{xz})}{\partial z} = 0 \qquad (4.3)$$

$$\frac{\partial(\bar{\rho}\tilde{w}\tilde{u} - \bar{t}_{xz} - \tau_{xz})}{\partial x} + \frac{\partial(\bar{\rho}\tilde{w}\tilde{v} - \bar{t}_{yz} - \tau_{yz})}{\partial y} + \frac{\partial(\bar{\rho}\tilde{w}^2 + p - \bar{t}_{zz} - \tau_{zz})}{\partial z} = 0 \qquad (4.4)$$

$$\frac{\partial\left[(\bar{\rho}\tilde{u}h_t - u(\bar{t}_{xx} + \tau_{xx}) - \nu(\bar{t}_{xy} + \tau_{xy}) - w(\bar{t}_{xz} + \tau_{xz}) + q_{Lx} + q_{Tx})\right]}{\partial x} +$$

$$\frac{\partial\left[(\bar{\rho}\tilde{v}h_t - u(\bar{t}_{xy} + \tau_{xy}) - \nu(\bar{t}_{yy} + \tau_{yy}) - w(\bar{t}_{yz} + \tau_{yz}) + q_{Ly} + q_{Ty})\right]}{\partial y} +$$

$$\frac{\partial\left[(\bar{\rho}\tilde{w}h_t - u(\bar{t}_{xz} + \tau_{xz}) - \nu(\bar{t}_{yz} + \tau_{yz}) - w(\bar{t}_{zz} + \tau_{zz}) + q_{Lz} + q_{Tz})\right]}{\partial z} = 0 \qquad (4.5)$$

$$t_{xx} = \frac{2}{3}\mu(2\frac{\partial\tilde{u}}{\partial x} - \frac{\partial\tilde{v}}{\partial y} - \frac{\partial\tilde{w}}{\partial z}) \, , \, t_{yy} = \frac{2}{3}\mu(2\frac{\partial\tilde{v}}{\partial y} - \frac{\partial\tilde{u}}{\partial x} - \frac{\partial\tilde{w}}{\partial z}) \, , \, t_{zz} = \frac{2}{3}\mu(2\frac{\partial\tilde{v}}{\partial y} - \frac{\partial\tilde{u}}{\partial x} - \frac{\partial\tilde{w}}{\partial z}) \, ,$$

$$t_{xy} = \mu(\frac{\partial\tilde{u}}{\partial y} + \frac{\partial\tilde{v}}{\partial x}) \, , \, t_{yz} = \mu(\frac{\partial\tilde{v}}{\partial z} + \frac{\partial\tilde{w}}{\partial y}) \, , \, t_{xz} = \mu(\frac{\partial\tilde{w}}{\partial x} + \frac{\partial\tilde{u}}{\partial z}) \, , \, \mu \equiv molecular \; viscosity \quad (4.6)$$

$$\tau_{xx} = \frac{2}{3}\mu_T(2\frac{\partial\tilde{u}}{\partial x} - \frac{\partial\tilde{v}}{\partial y} - \frac{\partial\tilde{w}}{\partial z}) \, , \, \tau_{yy} = \frac{2}{3}\mu_T(2\frac{\partial\tilde{v}}{\partial y} - \frac{\partial\tilde{u}}{\partial x} - \frac{\partial\tilde{w}}{\partial z}) \, , \, \tau_{zz} = \frac{2}{3}\mu_T(2\frac{\partial v}{\partial y} - \frac{\partial u}{\partial x} - \frac{\partial w}{\partial z}) \, ,$$

$$\tau_{xy} = \mu_T(\frac{\partial\tilde{u}}{\partial y} + \frac{\partial\tilde{v}}{\partial x}) \, , \, \tau_{yz} = \mu_T(\frac{\partial\tilde{v}}{\partial z} + \frac{\partial\tilde{w}}{\partial y}) \, , \, \tau_{xz} = \mu_T(\frac{\partial\tilde{w}}{\partial x} + \frac{\partial\tilde{u}}{\partial z}) \, , \, \mu_T \equiv Eddy \; viscosity \quad (4.7)$$

$$q_{Tx} = -\frac{\mu_T}{Pr_T}C_p\frac{\partial\tilde{T}}{\partial x} \; , \; q_{Ty} = -\frac{\mu_T}{Pr_T}C_p\frac{\partial\tilde{T}}{\partial y} \; , \; q_{Tz} = -\frac{\mu_T}{Pr_T}C_p\frac{\partial\tilde{T}}{\partial z} \; ,$$

$$q_{Lx} = -\frac{\mu}{Pr_L}C_p\frac{\partial\tilde{T}}{\partial x} \; , \; q_{Ly} = -\frac{\mu}{Pr_L}C_p\frac{\partial\tilde{T}}{\partial y} \; , \; q_{Lz} = -\frac{\mu}{Pr_L}C_p\frac{\partial\tilde{T}}{\partial z}$$

$$C_p \equiv Pressure \; coefficient \, , \; Pr_T \equiv Turbulent \; Prandtl \; number$$

$$Pr_L \equiv Laminar \; Prandtl \; number \tag{4.8}$$

$$P = \bar{\rho}R\bar{T} \tag{4.9}$$

$$e_t = \tilde{e} + \frac{1}{2}(\tilde{u}^2 + \tilde{v}^2 + \tilde{w}^2) \tag{4.10}$$

$$h_t = e_t + \frac{P}{\tilde{\rho}} \tag{4.11}$$

4.2 Turbulence Models

Each turbulence model has advantages and disadvantages. The k-ϵ model is the most widely used turbulence model, but does not perform well in adverse pressure gradients and wall-bounded flows [33]. Further, the k-ϵ model does not compare well with wing/body experimental data [44]. The Spalart-Allmaras model has been calibrated for airfoils and wings, but has poor performance predicting separated flows [33].

The turbulence models used for this study are the Wilcox 1998 k-ω and the Menter 1994 k-ω SST models. They show good behavior in an adverse pressure gradient and have good

comparison with wing-body juncture experiments [33],[34].

4.2.1 Wilcox 1998 k-ω Model

The k-ω model uses equations 4.12 and 4.13 to simultaneously solve for Turbulent Kinetic Energy , k, and the Specific Dissipation Rate, ω. The turbulent and effective viscosities along with the closure coefficients are given by equations 4.14 and 4.15, respectively. The χ functions for k and ω are given by equations 4.16 while the Production term P is given by equation 4.17.

$$\phi_{k'} = k \; , \; D_k = \frac{\partial}{\partial x_j}\left(\mu_{eff,k}\frac{\partial k}{\partial x_j}\right) \; , \; S_{Pk} = \bar{\rho}P \; , \; S_{Dk} = \beta^*\bar{\rho}k\omega \; , \; S_A = 0 \tag{4.12}$$

$$\phi_{\omega'} = \omega \; , \; D_\omega = \frac{\partial}{\partial x_j}\left(\mu_{eff,\omega}\frac{\partial \omega}{\partial x_j}\right) \; , \; S_{Pk} = \bar{\rho}P \; , \; S_{P\omega} = \bar{\rho}\frac{\gamma}{\nu_t}P \; , \; S_{D\omega} = \beta\bar{\rho}\omega^2 \tag{4.13}$$

$$\mu_{eff,k} = \mu + \sigma_k\mu_t \; , \; \mu_{eff,\omega} = \mu + \sigma_\omega\mu_t \; , \; \mu_t = \bar{\rho}k/\omega \tag{4.14}$$

$$\alpha = \frac{13}{25} \; , \; \beta = \beta_o f_\beta \; , \; \beta^* = \beta_o^* f_\beta \; , \; \sigma_k = \sigma_\omega = \frac{1}{2} \; , \; \beta_0^* = \frac{9}{100} \; ,$$

$$f_\beta = \frac{1 + 70\chi_\omega}{1 + 80\chi_\omega} \; , \; \chi_\omega \equiv \left|\frac{\Omega_{ij}\Omega_{jk}S_{ki}}{(\beta_o^*\omega)^3}\right| \; , \; \beta_o = \frac{9}{125}$$

$$f_{\beta^*} = \begin{cases} 1, & \chi_k \leq 0 \\ \frac{1+680\chi_k^2}{1+400\chi_k^2} & \chi_k > 0 \end{cases} \; , \; \chi_k \equiv \frac{1}{\omega^3}\frac{\partial k}{\partial x_j}\frac{\partial \omega}{\partial x_j} \; , \tag{4.15}$$

$$\chi_k = \frac{1}{\omega^3}\left|\left(\frac{\partial k}{\partial x}\frac{\partial \omega}{\partial x} + \frac{\partial k}{\partial y}\frac{\partial \omega}{\partial y} + \frac{\partial k}{\partial z}\frac{\partial \omega}{\partial z}\right)\right.$$

$$\chi_\omega = \frac{1}{4(\beta_0^*\omega)^3}\left(\frac{\partial \tilde{v}}{\partial x} - \frac{\partial \tilde{u}}{\partial y}\right)\left(\frac{\partial \tilde{u}}{\partial y} - \frac{\partial \tilde{v}}{\partial x}\right)\left(\frac{\partial \tilde{v}}{\partial x} + \frac{\partial \tilde{\mu}}{\partial y}\right) +$$

$$\left(\frac{\partial \tilde{w}}{\partial x} - \frac{\partial \tilde{u}}{\partial y}\right)\left(\frac{\partial \tilde{u}}{\partial y} - \frac{\partial \tilde{w}}{\partial x}\right)\left(\frac{\partial \tilde{u}}{\partial x} + \frac{\partial \tilde{w}}{\partial y}\right) + \left(\frac{\partial \tilde{w}}{\partial x} - \frac{\partial \tilde{v}}{\partial y}\right)\left(\frac{\partial \tilde{v}}{\partial y} - \frac{\partial \tilde{w}}{\partial x}\right)\left(\frac{\partial \tilde{v}}{\partial x} + \frac{\partial \tilde{w}}{\partial y}\right)$$

$$+ \left(\frac{\partial \tilde{w}}{\partial x} - \frac{\partial \tilde{u}}{\partial y}\right)\left(\frac{\partial \tilde{v}}{\partial y} - \frac{\partial \tilde{w}}{\partial x}\right)\left(\frac{\partial \tilde{v}}{\partial x} + \frac{\partial \tilde{u}}{\partial y}\right) + \left(\frac{\partial \tilde{v}}{\partial x} - \frac{\partial \tilde{u}}{\partial y}\right)\left(\frac{\partial \tilde{w}}{\partial y} - \frac{\partial \tilde{v}}{\partial x}\right)\left(\frac{\partial \tilde{w}}{\partial x} + \frac{\partial \tilde{u}}{\partial y}\right)$$

$$\left(\frac{\partial \tilde{u}}{\partial x} - \frac{\partial \tilde{v}}{\partial y}\right)\left(\frac{\partial \tilde{w}}{\partial y} - \frac{\partial \tilde{u}}{\partial x}\right)\left(\frac{\partial \tilde{w}}{\partial x} + \frac{\partial \tilde{v}}{\partial y}\right)\Bigg| \tag{4.16}$$

$$P = \mu_T\left\{2\left[\left(\frac{\partial \tilde{u}}{\partial x}\right)^2 + \left(\frac{\partial \tilde{v}}{\partial y}\right)^2 + \left(\frac{\partial \tilde{w}}{\partial z}\right)^2\right] + \left(\frac{\partial \tilde{u}}{\partial y} + \frac{\partial \tilde{v}}{\partial x}\right)^2 + \left(\frac{\partial \tilde{u}}{\partial z} + \frac{\partial \tilde{w}}{\partial x}\right)^2 + \left(\frac{\partial \tilde{v}}{\partial z} + \frac{\partial \tilde{w}}{\partial x}\right)^2\right\}$$

$$-\frac{2}{3}\mu_T\left(S_{kk}\right)^2 - \frac{2}{3}\rho k S_{kk}\,, \quad where \quad S_{kk} = \frac{\partial \tilde{u}}{\partial x} + \frac{\partial \tilde{v}}{\partial y} + \frac{\partial \tilde{w}}{\partial z} \tag{4.17}$$

4.2.2   Menter 1994 k-ω Shear Stress Transport

The Menter 1994 k-ω Shear Stress Transport (SST) model combines the strengths of the k-ω and k-ϵ models. The k-ω model compares with experimental measurements of wall bounded flows while the k-ϵ model works best far from the wall [35],[20]. The k-ϵ model is converted into a k-ω formulation and both are incorporated into the k-ω SST. The formulation allows the k-ω model to be used near the wall and the k-ϵ model to be used away from the wall where each is most robust. The transformed k-ω SST model can be seen in equations 4.18 and 4.19. The constants used in the k-ω and k-ϵ are transformed by equation 4.20 with closure coefficients given by equation 4.21 along with definitions of equations given by equations 4.22.

$$\frac{D\rho k}{Dt} = \tau_{ij}\frac{\partial u_i}{\partial x_j} - \beta^*\rho\omega k + \frac{\partial}{\partial x_j}\left[(\mu + \sigma_k\mu_t)\frac{\partial k}{\partial x_j}\right] \tag{4.18}$$

$$\frac{D\rho\omega}{Dt} = \frac{\gamma}{\nu_t}\tau_{ij}\frac{\partial u_i}{\partial x_j} - \beta\rho\omega^2 + \frac{\partial}{\partial x_j}\left[(\mu + \sigma_\omega\mu_t)\frac{\partial\omega}{\partial x_j}\right] + 2\rho\left(1 - F_1\right)\sigma_{\omega 2}\frac{1}{\omega}\frac{\partial k}{\partial x_j}\frac{\partial\omega}{\partial x_j} \tag{4.19}$$

$$\phi = F_1\phi_1 + (1 - F_1)\phi_2 \tag{4.20}$$

$$\sigma_{k1} = 0.85\,,\;\; \sigma_{\omega 1} = 0.5\,,\;\; \beta_1 = 0.0750\,,\;\; a_1 = 0.31\,,\;\; \beta^* = 0.09\,,$$

$$\kappa = 0.41\,,\;\; \gamma_1 = \beta_1/\beta^* - \sigma_{\omega 1}\kappa^2/\sqrt{\beta}^2 \tag{4.21}$$

$$\nu_t = \frac{a_1 k}{max(a_1\omega; \Omega F_2)}\,,\;\; F_1 = tanh(arg_1^4)\,,\;\; F_2 = tanh(arg_2^2)\,,$$

$$arg_2 = max\left(2\frac{k^{0.5}}{0.09\omega y}; \frac{500\nu}{y^2\omega}\right)\,,\;\; P_\omega = \gamma\frac{\omega}{k}\tau_{ij}\frac{\partial u_i}{\partial x_j}\,,$$

$$\tau_{ij} = \mu_t\left(\frac{\partial u_i}{\partial x_j} + \frac{\partial u_j}{\partial x_i} - \frac{2}{3}\frac{\partial u_k}{\partial x_k}\delta_{ij}\right)\,,\;\; arg_1 = min\left[max\left(\frac{k^{0.5}}{0.09\omega y}; \frac{500\nu}{y^2\omega}\right); \frac{4\rho\sigma_{\omega 2}k}{CD_{k\omega}y^2}\right] \tag{4.22}$$

4.3 Discretization Procedure

The flow is discretized using Finite Volume Method (FVM) along with Roe's upwind scheme [45]. The FVM calculates the fluxes at cell faces using the values given at cell centers. The discretization scheme uses second-order-upwind Monotone Upstream-centered Schemes

for Conservation Laws (MUSCL) extrapolation [20]. This allows shocks to be accurately captured over just a few cells.

4.4   Grid

Grids, or meshes, are the method by which the domain of interest is discretized. For finite volume methods the domain is divided into cells. The two main types of grids are structured and unstructured, where structured grids have a clear order to their arrangement and unstructured grids have no clear order [21].

This study uses structured grids to mesh the specified geometry. A two-dimensional example can be seen in Figure 4.1. Note the cells acquire large aspect ratios and skewness in the process of meshing the geometry due to the geometry of the test article and the tight spacing required near the wall. If the aspect ratios and skewness become too large they can affect grid quality. Therefore, grids must be carefully generated to avoid issues. The commercial program Gridgen by Pointwise (TM) was used to create the grids [46]. Gridgen is a common mesh generator in industry and the main grid generator for CFD applications in the Aerospace and Ocean Engineering Department at Virginia Tech.

The grid employed is a fully structured grid with 69 blocks and 44.4 million cells with a $y^+ < 0.5$. The purpose of this study is to accurately capture junction flows. To achieve this, the laminar sublayer of the boundary layer must be modeled. The laminar sublayer is measured in units of y^+, which is formulated in equation 4.23. For the laminar sublayer to be properly modeled, the maximum y^+ value should be below 1.0. The finest grid is
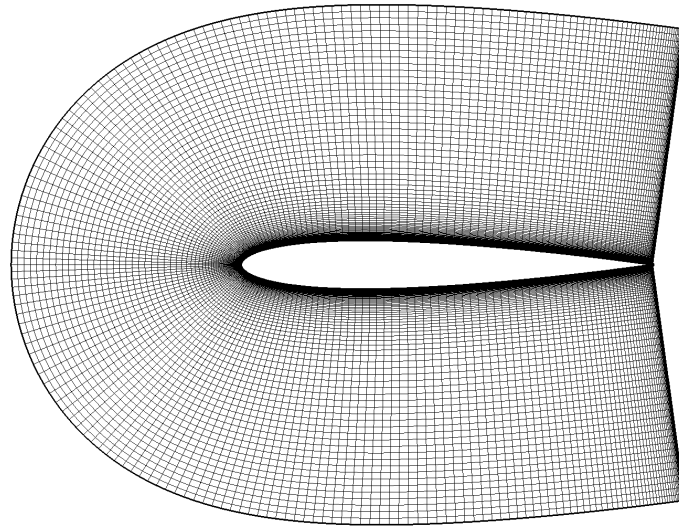
Figure 4.1: Example of a grid enveloping a NACA 0012 airfoil.

systematically coarsened by a factor of 4/3, 2, and 4 to produce a family of grids, as seen in

Table 4.1. Only the coarsest grid has a $y^+ > 1.0$. A grid study, seen in Chapter 6, shows

the 18.8 million cell grid has the best combination of accuracy and computational time for

multiple parametric runs.

$$y^+ = \frac{yu_*}{\nu} \ \ where \ u_* = U_e\sqrt{\frac{C_f}{2}} \tag{4.23}$$

Table 4.1: Grid family information

Name	Grid Cells	Grid Refinement
Coarse	700K	4.00
Medium	5.8M	2.00
Fine	18.8M	1.33
Finest	44.4M	1.00

Chapter 5

Verification

5.1 Code Verification

Mistakes in a CFD code can lead to inaccuracies in solutions. Human error accounts for many problems with coded algorithms [47]. Code verification is the process of assessing a code to ensure the governing equations are solved correctly by the algorithm. CFD codes must be verified against a known solution or benchmark case. There are several methods of comparing these two solutions with order of accuracy tests being the most rigorous.

5.1.1 Order of Accuracy

The formal order of accuracy is the theoretical rate of convergence of the discrete solution to the exact solution to the mathematical model. The observed order of accuracy is calculated from a series of systematically refined grids [12].

5.1.2   ANSYS Fluent Verification

The procedure for verifying CFD codes involves using the Method of Manufactured Solutions (MMS), exact solutions, or benchmark cases [12]. The known solution is compared against the numerical solution. Code verification studies have been performed in Fluent for the Euler equations and the RANS equations with the k-ω SST model [48]. The Euler equations were verified using the exact solution to Ringlebs flow and approached second order accuracy. The k-ω SST model was tested for a flat plate using a code to code comparison. The comparison uses NASAs verified CFL3D and FUN3D codes [44]. The Fluent solutions asymptote toward the flat plate solutions. The coefficient of drag for the two codes disagree by 0.000821%.

5.2   Solution Verification

Solution verification quantifies the numerical errors created by discretizing and solving the governing equations over the domain. This is performed by assessing the round off, statistical sampling, iterative, and discretization errors [12]. Round off error is due to the finite precision of computers and is generally assessed by running a test case at two levels of precision. The grids run in this study require double precision. Since ANSYS Fluent does not have any higher lever of precision, round off error could not be assessed for this study. However, it is typically much smaller than the other forms of error [12]. Therefore it is assumed to have a negligible effect on the final solution. Statistical sampling error is

only important when a SRQ oscillates slightly about a particular solution. There was no oscillation, so this was not necessary for this study.

5.2.1 Iterative Error

Iterative error is defined as the difference between the current approximate solution to the discretized governing equations and the solution to the discretized governing equations given infinite computing power and time [12]. Since the latter is unattainable, iterative error is estimated by keeping a history of the drag as the solution iteratively converged. The iterative error was calculated using equation 5.1. Figure 5.1 is an example of an iterative error history. The iterative error (IE Cd) decreases through the domain, but does not show a decrease below 0.01% due to the finite precision of the force output of 5 significant figures. A conservative iterative error estimate for Figure 5.1 is 0.05%, which is an acceptable value for this study.

$$IE = \left| \frac{C_{d\,Iteration} - C_{d\,Final}}{C_{d\,Final}} \right| \tag{5.1}$$

5.2.2 Discretization Error

Discretization error, ε_h , is defined by equation 5.2. ε_h is the difference between the exact solution to the discretized equations and the exact solution to the governing equations [12]. It is generally the largest numerical error and the hardest to estimate. There are several methods that can be used to estimate ε_h, most of which are code intrusive. The Grid
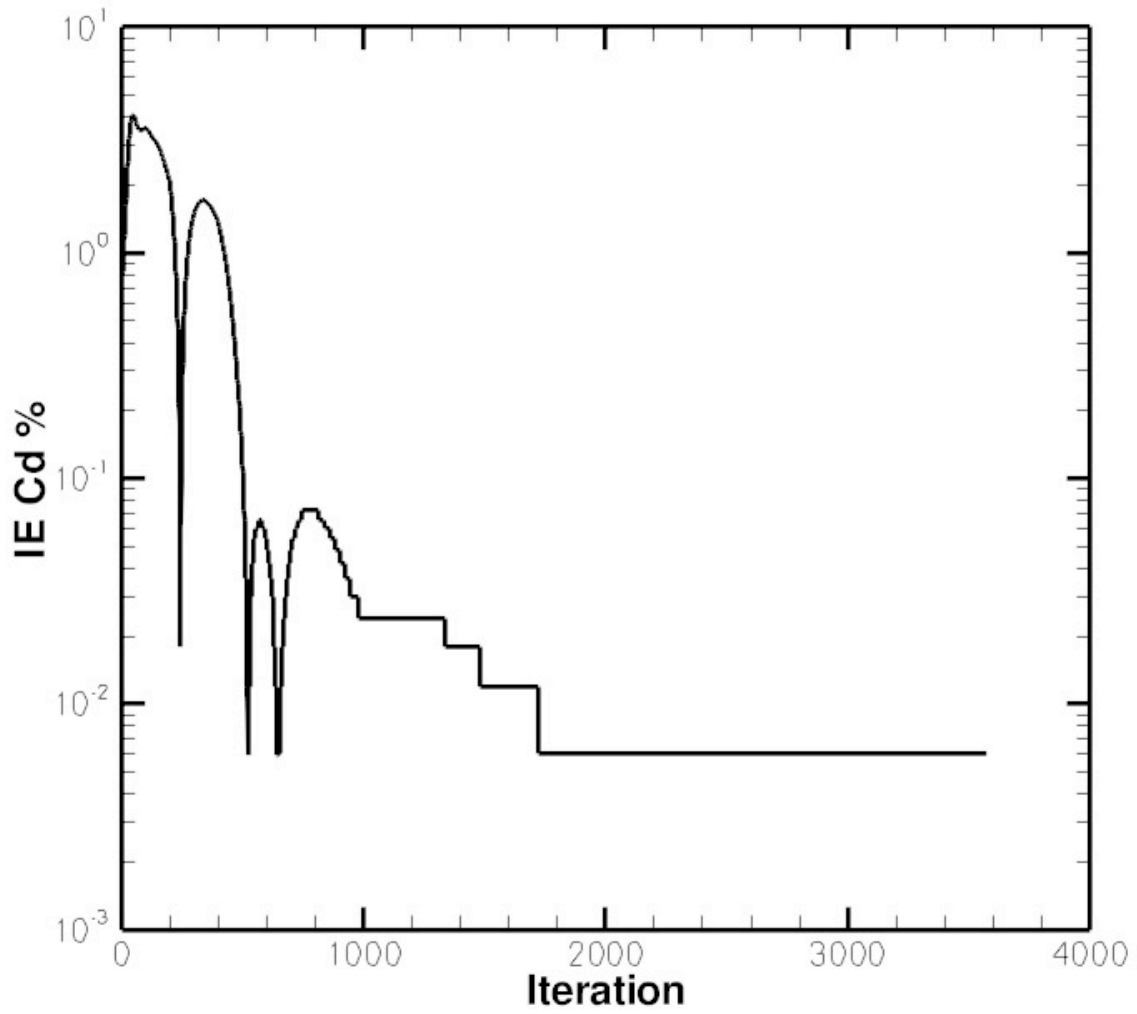
Figure 5.1: Percent iterative error versus iteration is seen as IE Cd.

Convergence Index (GCI) is used for this study since the source code for ANSYS Fluent is

unavailable.

$$\varepsilon_h = u_h - \tilde{u} \tag{5.2}$$

Richardson extrapolation is the basis for the GCI. The goal of the GCI is to achieve 95%

certainty that discretization error falls within the resulting numerical uncertainty bands.

Richardson extrapolation uses two solutions to extrapolate to a more accurate higher order

solution [49]. A major assumption of Richardson extrapolation is the solutions are in the

asymptotic range. The asymptotic range is where the leading truncation error terms domi-

nate the discretization error. Discretization error is estimated by equation 5.3, where f_i is a

calculated solution and $\bar{f}$ is an extrapolated solution. The GCI uses ε_h and makes an esti-

mate of the discretization uncertainty, since the two solutions may not be in the asymptotic

range. Equation 5.4 shows the version of the GCI used in this study.

$$\varepsilon_h = f_i - \bar{f} \tag{5.3}$$

$$GCI = \frac{F_s}{r^p - 1} \left| f_i - \bar{f} \right| \tag{5.4}$$

To fully estimate the discretization uncertainty, the GCI requires the following: two so-

lutions, f_1 and f_2, must be calculated on two systematically refined grids with refinement

factor r. The observed order of accuracy, p, must be calculated using at least three system-

atically refined grids. The factor of safety (F_s) is either 1.25 or 3 depending how close the

observed order of accuracy is to the formal order of accuracy. Typically, the observed and formal order of accuracy must be within ten percent of each other to use $F_s = 1.25$, but this system has an inherent singularity seen in the shock on top of the fin. The effect of a flow singularity on observed order of accuracy is an open research question, but studies show the observed order of accuracy ultimately reduces to first order with sufficient refinement [12]. For this study F_s is chosen using the following method. Observed orders of accuracy between first and second order are sufficient to constitute $F_s = 1.25$. If $1 \leq p \leq 2$, then $F_s = 1.25$ and $p = p_{observed}$. If this is not the case, then $F_s = 3.0$ and p is determined by $p_{observed}$. If $p_{observed} < 1$ then $p = 1$, if $p_{observed} > 2$ then $p = 2$.

5.3 Grid Study

The grid study involved a single grid family at two angles of attack, 0° and 5°, all of which were systematically refined. The observed order of accuracy was calculated for the two finest grids. Order of accuracy calculations require three grids, so the fine grid along with the two immediate coarser grids were used for each calculations. The results can be see in Table 5.1.

Since the observed order of accuracy does not match the formal order of accuracy, a factor of safety of 3.0 is used for the GCI. The Numerical Uncertainty (NU) for the SRQs can be seen in Table 5.2. The grid study shows $NU < 10\%$ for all cases, except for LE at angle of attack 5°, which has $NU = 37.84\%$.

Table 5.1: Observed Order of Accuracy

Angle of Attack 0°		
Grid Reference Length	Observed Order of Accuracy	Grids Used to Compute p
1.333	5.099	Coarse, Medium, Fine
1.000	Oscillatory	Medium, Fine, Finest
Angle of Attack 5°		
Grid Reference Length	Observed Order of Accuracy	Grids Used to Compute p
1.333	2.359	Coarse, Medium, Fine
1.000	2.564	Medium, Fine, Finest

Table 5.2: Numerical Uncertainties

	SRQs	Fine Grid Value	Numerical Uncertainty (%)
	C_d	0.00413	2.89
Angle of Attack 0°	LE	0.8284	1.26
	Max Span	6.536E-3	0.23
	Span at 88.8%	6.536E-3	0.23
	SRQs	Fine Grid Value	Numerical Uncertainty (%)
	C_d	0.01578	6.62
Angle of Attack 5°	LE	0.1491	37.84
	Max Span	0.1599	3.14
	Span at 88.8%	0.1567	2.50

Chapter 6

Results

6.1   2D Data Comparisons

Two dimensional data was obtained from the ATAT program using a NACA 0012 placed in the 0.3 meter cryogenic transonic tunnel at NASA Langley [24]. Note, the ATAT program's aim was to obtain experimental data for the two dimensional airfoil behavior in the freestream. The wind tunnel approximated this behavior by using an unswept wing across the span of the tunnel and employing porous walls at the top and bottom of the tunnel.

The experimental data was then compared to CFD data of the same airfoil (NACA 0012) at the same Mach and Reynolds number. The airfoil was assumed to be 2D and in the freestream (tunnel walls neglected). A comparison of the C_p plots can be seen in Figure 6.1. The results show good agreement for both angles of attack. The shock locations are the same for CFD and experiment. There is a noticeable difference between CFD and
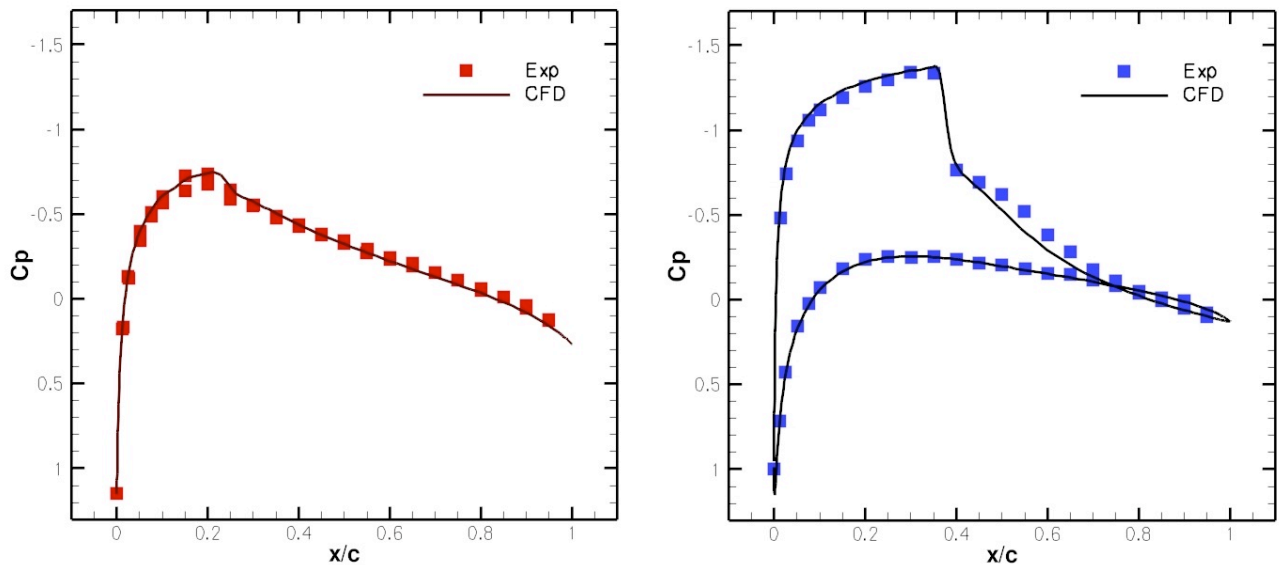
Figure 6.1: Comparison of experimental and CFD data for a 2-D NACA 0012 at M=0.76 and Re = 6.0 million and angle of attack 0° and 4° respectively.

experiment behind the shock at angle of attack 4°. It appears CFD slightly under predicts separation effects. The discrepancy is notable, but not substantial.

6.2   Turbulence Model Comparison

A short study was performed to see how the different turbulence models available in ANSYS Fluent 12.0 compared to each other. Table 6.1 shows SRQ results while Table 6.2 shows the error based on the k-ω SST model. The comparison was performed on a 5.8 million cell grid at angle of attack 4°. The short study shows the k-ω and Spalart Allmaras models comparing well with the k-ω SST while the k-ϵ realizable produces similar behavior, but does not compare as well. It is worth noting that the k-ϵ realizable case had poor iterative

residual behavior and the iterative error was greater than 1%.

Table 6.1: The effect of Turbulence Models on SRQs for Angles of Attack 4°

Turbulence Models	C_D	LE (x/c)	Max Span (y/b)	Span 88.8%
k-ω SST	0.01279	18.30	14.91	14.91
k-ω	0.01280	18.29	14.89	14.88
Spalart Allmaras	0.01333	16.35	15.43	15.63
k-ϵ realizable	0.01686	21.29	12.13	12.09

Table 6.2: % Error based on k-ω SST SRQs for Angles of Attack 4°

Turbulence Models	C_D	LE (x/c)	Max Span (y/b)	Span 88.8%
k-ω	0.11	0.04	0.17	0.21
Spalart Allmaras	4.24	10.68	3.44	3.48
k-ϵ realizable	31.83	16.35	18.68	18.88

6.3   Interference Drag Estimation

It is important to isolate the drag in the interaction region. It is assumed that the drag will increase when a separation zone appears. If this is shown as a CFD result it will add evidence to this assumption. A major limitation of this method is that it cannot be compared to experimental measurements.
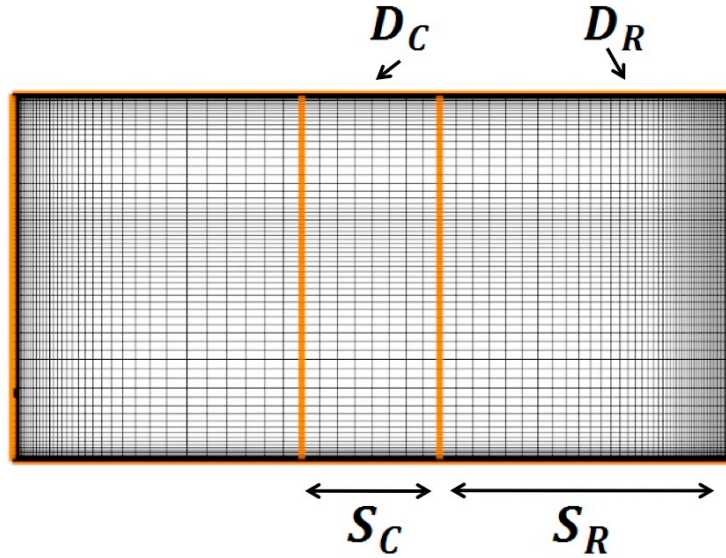
Figure 6.2: The breakdown of the fin computationally into left, center, and right components.

The measurement of interference drag is performed by breaking the fin into different segments as seen in Figure 6.2. The segments are the left, center, and right where the drag is dominated by induced drag, nominal 2-D drag, and interference drag respectively. The center of the span is assumed to be 2-D, though we might see different behavior if the fin extended across the test section. The right segment is exposed to the side wall boundary layer. This means there is a lower Mach number and therefore lower drag. The interference drag is calculated using equation 6.1 where $D_{interference}$ is the actual interference drag, D_i is the drag on the segment i, and S_i is the surface area of the segment i.

$$D_{interference} \approx D_R - \frac{S_R}{S_C} D_C \qquad (6.1)$$

The interference drag is studied at angle of attack 3° before and after the bifurcation

point of the separation. The coefficient of interference drag is estimated by the calculated interference drag and using the reference area of chord squared (c^2), as used by Duggirala, et al [11]. For low separation $C_{D_{int}} = -0.0017$. This value is negative due to the large boundary layer which decreases the apparent Mach number near the wall. For high separation $C_{D_{int}} = 0.0022$. The difference between these is $C_{D_{int}} = 0.0039$ or 39 drag counts.

6.4 Uncertainty Propagation Methods

6.4.1 Aleatory and Epistemic Uncertainty

There are two main types of uncertainty, aleatory and epistemic. Aleatory uncertainty is an uncertainty which has a known probability distribution. The typical probability distribution is a normal or Gaussian distribution, though there are others. Epistemic uncertainty is when the uncertainty is due to a lack of knowledge. In this case the uncertainty can only be bounded. The true value can lie anywhere within the bounds, but no probability distribution is known.

For real world applications there is a mixture of aleatory and epistemic uncertainties. This study has narrowed down the known model input uncertainties to changes in Reynolds number, freestream Mach number, and tunnel wall boundary layer growth as the test runs. Of these quantities, Mach and Reynolds number are treated as aleatory uncertainties while boundary layer growth is treated as an epistemic uncertainty. A sensitivity study has shown the interaction region is insensitive to changes in Reynolds number, but is sensitive to

freestream Mach number and boundary layer growth. The experiments report that the uncertainty in the Mach number is normally distributed with a mean of $M = 0.75$ and a standard deviation of 0.01 [41]. The boundary layer is characterized by previous studies and theoretical models, but its growth is not precisely known. Therefore, the boundary layer growth is considered an epistemic uncertainty and treated as an interval. Uncertainties due to the turbulence model and the use of solid walls in the simulations (as opposed to the porous walls used in the experiment) will be estimated later as part of model form uncertainty.

6.4.2   Cumulative Distribution Functions

A Cumulative Distribution Function (CDF) is one method of characterizing the uncertainty in a SRQ. The CDF is the integral of the the Probability Density Function (PDF) [12]. A comparison between the two can be seen in Figure 6.3. The CDF is read as a cumulative probability whose a value is less than or equal to a given value. For example, in Figure 6.3 the cumulative probability that the thermal conductivity is less than or equal to $0.6 \, W/m -^\circ C$ is 50%.

In many cases there may be a nonlinearity in the SRQs as they are being sampled for the CDF. The point at which the behavior changes is called a bifurcation point. This study has such a case, for certain angles of attack the separation behavior in the interaction region can change rapidly with small changes in Mach number. For these cases the CDF can change from its normal appearance to resemble Figure 6.4.
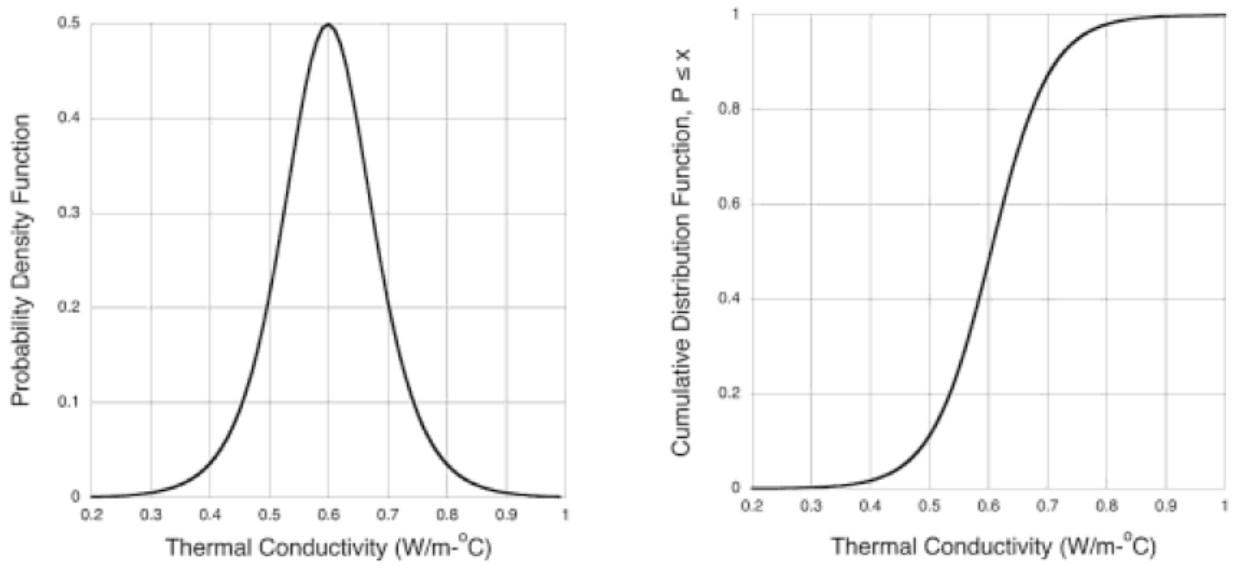
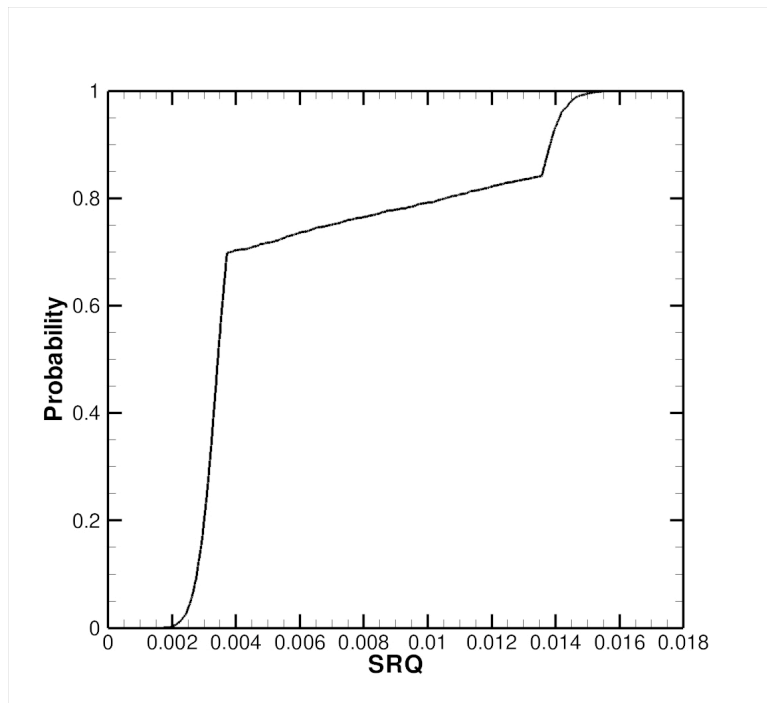Figure 6.3: Example of a PDF and CFD from Oberkampf and Roy [12].

Figure 6.4: Example of a CDF with a bifurcation point.

6.4.3   Probability Box

A probability box, or p-box, results when aleatory and epistemic uncertainties are propagated through a model. This can be performed by first using Latin hypercube sampling for the epistemic uncertainties, fixing the epistemic uncertainty at a particular value, and then cycling through the aleatory uncertainties using Monte Carlo sampling. Each sample of the epistemic uncertainties creates a conditional CDF; i.e., a CDF conditioned on the sampled value of the epistemic uncertainty. The widest extents of the ensemble of CDFs produce the bounds of the p-box. An example can be seen in Figure 6.5.

This study modifies these procedures for the specific problem. The only known epistemic uncertainty is the boundary layer growth. The boundary layer is known at the start of the tunnel run, but has been estimated for the end of the tunnel run, so bounds of the p-box are approximated by running only the beginning and ending boundary layers. The only relevant aleatory uncertain input is the Mach number. Multiple runs with all other conditions held the same, except for the Mach number, show a linear relationship between Mach number and the SRQs. The exception is when there is a rapid increase in separation zone size. This case shows a rapid change in all SRQs with Mach number. To model the changes, the simulation is run at several different Mach numbers close to the "bifurcation point." The behavior is linear before and after the bifurcation point. Interpolation is used at the bifurcation point since full simulation runs are expensive. The linear behavior of the SRQs is combined with the interpolation of the bifurcation point so the SRQs can be sampled multiple times to create a CDF. This produces a highly resolved CDF with minimal computational expense.
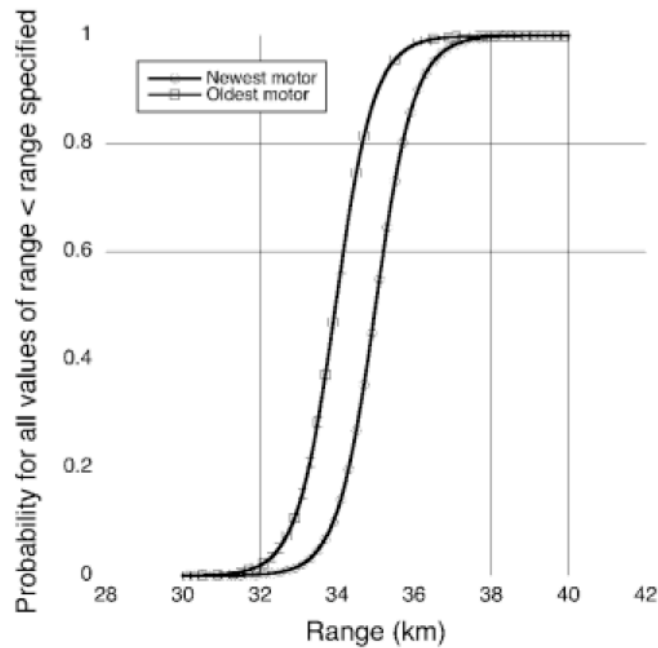
Figure 6.5: p-box example from Oberkampf and Roy [12].

In summary, for this study the epistemic uncertainty is reduced to only two boundary layer conditions and the Mach number can be easily related to the SRQ. The p-box bounds are produced by propagating the aleatory Mach number uncertainty through the model at both the beginning and ending tunnel boundary conditions.

6.5   System Response Quantities

The SRQs used in this study are limited by those measured experimentally. The data obtained in the experiment are sparse and limited to force and moment data along with oil flow visualization. Drag is the main force which changes as separation grows in the interaction region. The total drag includes drag due to lift, wave drag, viscous effects, and

interference drag. The change in total drag because of interference effects is slight. Therefore, the flow visualization data is mainly used for assessing turbulence models.

The separation zone in the interaction region has a large effect on the interference drag. A good assessment of the turbulence models is how well they predict this separation region. One qualitative comparison method is to visually compare experimental oil flow visualizations to near-surface streamlines created from simulations, seen in Figure 6.6. A more rigorous method is comparing specific measurements of the separation zone. These measurements are the start of separation from the leading edge (LE), the maximum span of the separation zone (Max Span), and the span of the separation zone at a specific chord length. The chord length is chosen where there is a grid line so there is no interpolation error. For parametric studies this location is chosen to be 88.8% chord (Span at 88.8%). A graphic representation of these SRQs can be seen in Figure 6.7.

6.6   Surface Flow vs. Angle of Attack

Figure 6.8 shows how the separation zone and strong shock vary with angle of attack. The Mach number and entrance boundary layer were the same: M=0.75 and the tunnel start boundary layer. For angle of attack 3°, the separation zone in the interaction region is very small. There is some slight separation behind the strong shock, but it has a maximum height of $3.0X10^{-5}$ meters. As the angle of attack increases to 4°, the strong shock and separation zone in the interaction region get much larger and change their behavior. The separation zone moves toward the leading edge and widens near the trailing edge. The strong
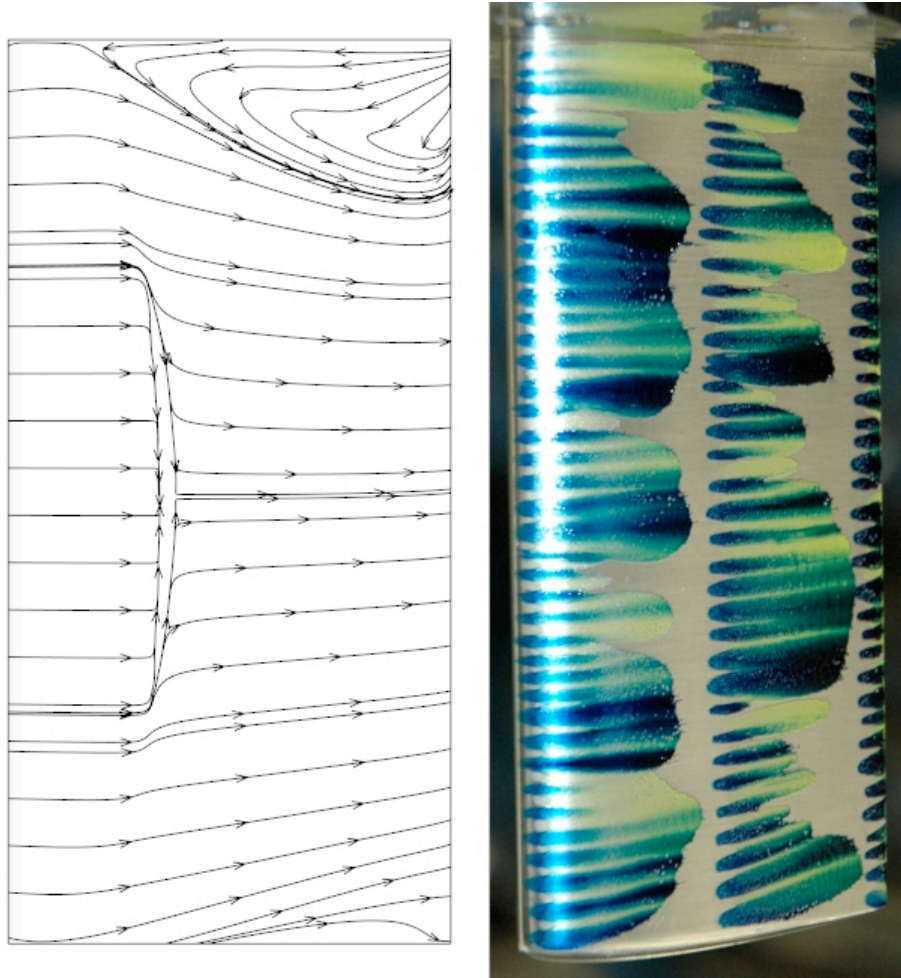
M = 0.75 , Re = 6 million

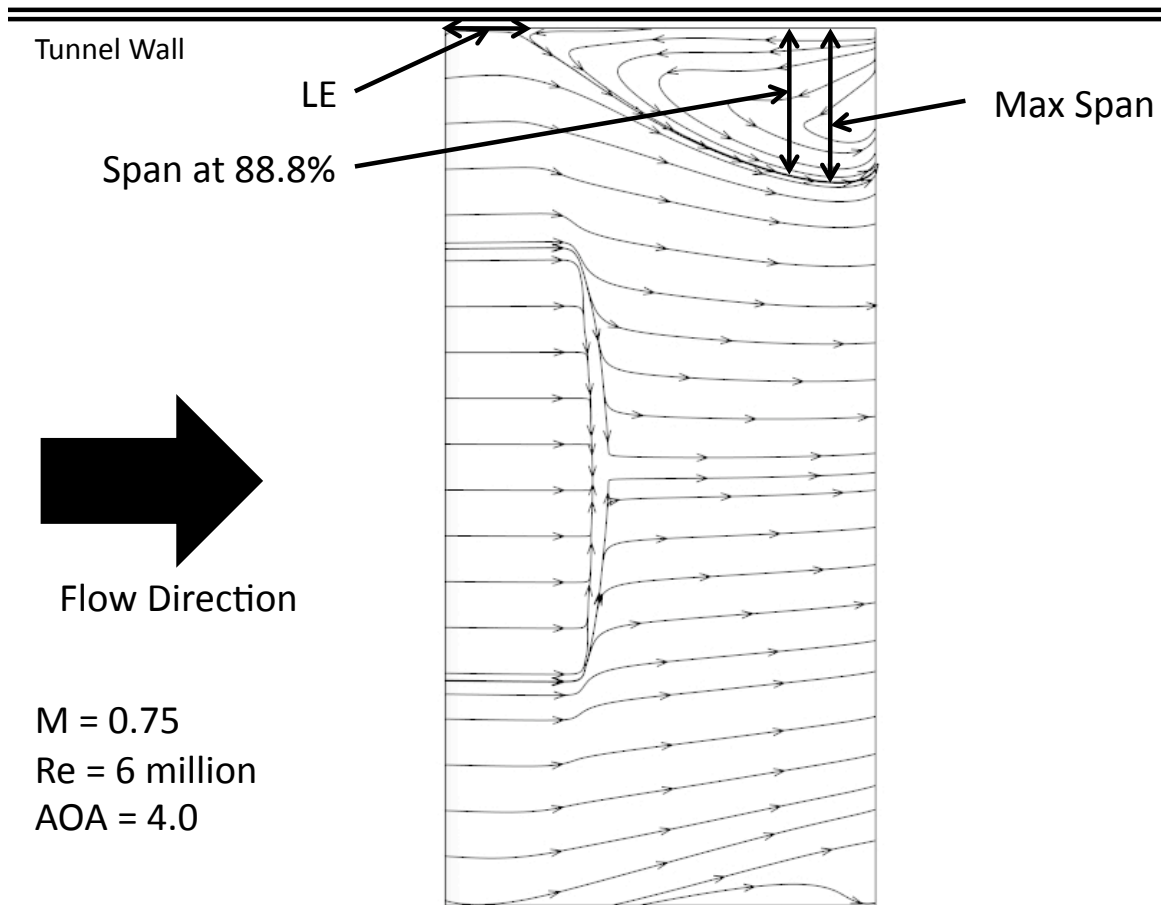Figure 6.6: Streamlines from CFD versus experimental oil flow visualization [41].

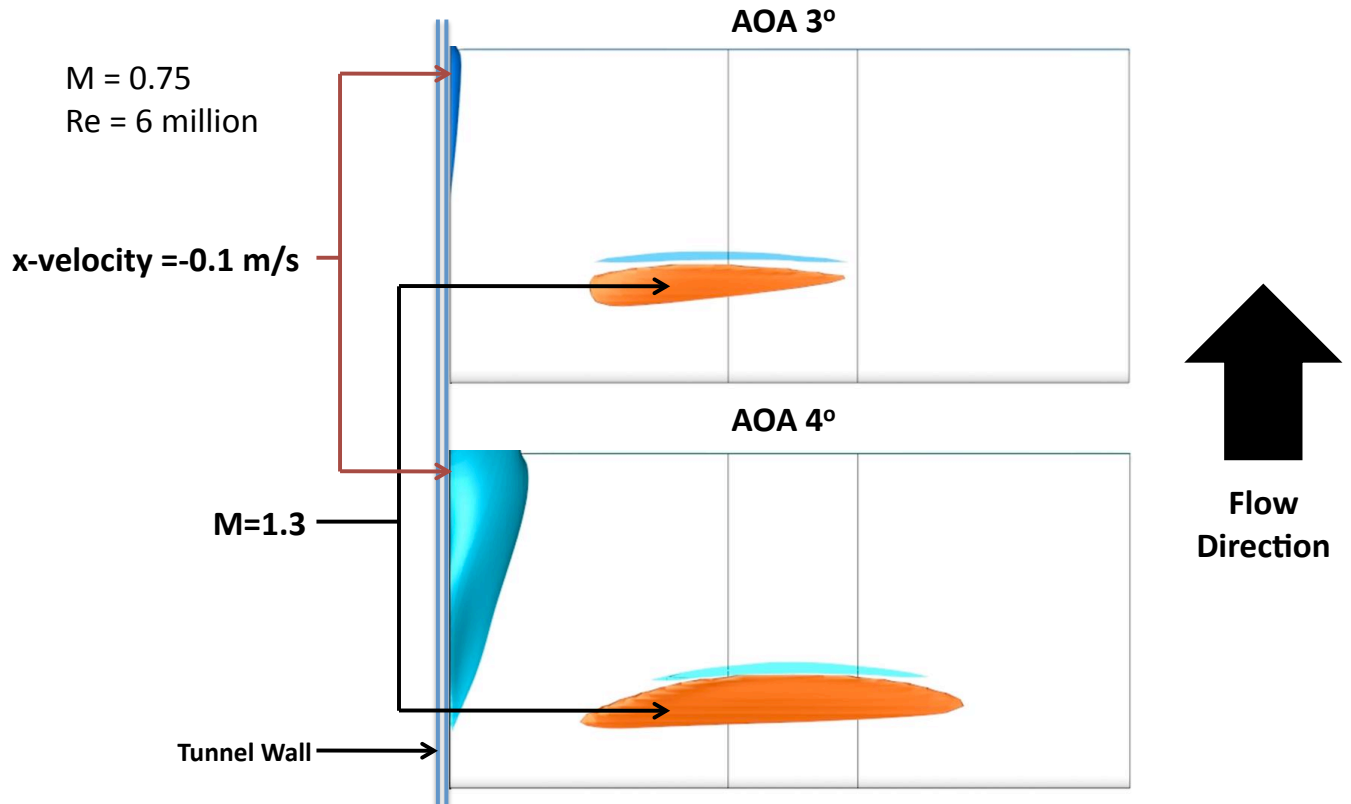Figure 6.7: Measurements of separation metrics.

Figure 6.8: Angles of attack 3° and 4° with isosurfaces showing strong shocks (M=1.3) and separation (x-velocity = -0.1m/s).

shock becomes more symmetrical due to the larger separation zone. The separation behind the strong shock becomes larger and symmetrical, but does not change height. Below angle of attack 3° the separation zone and shock strength continue to decrease. Above angle of attack 4° the shock strength grows while the separation zone in the interaction region does not change much.

Figure 6.9 shows streamlines near the surface obtained from CFD along with experimental data. At angle of attack 3° the shock is apparent from the recirculation zone along with disturbances in the streamlines. The recirculation zone in the interaction region is apparent,

AOA 3º

● UTA Separation Data

AOA 4º

M = 0.75
Re = 6 million
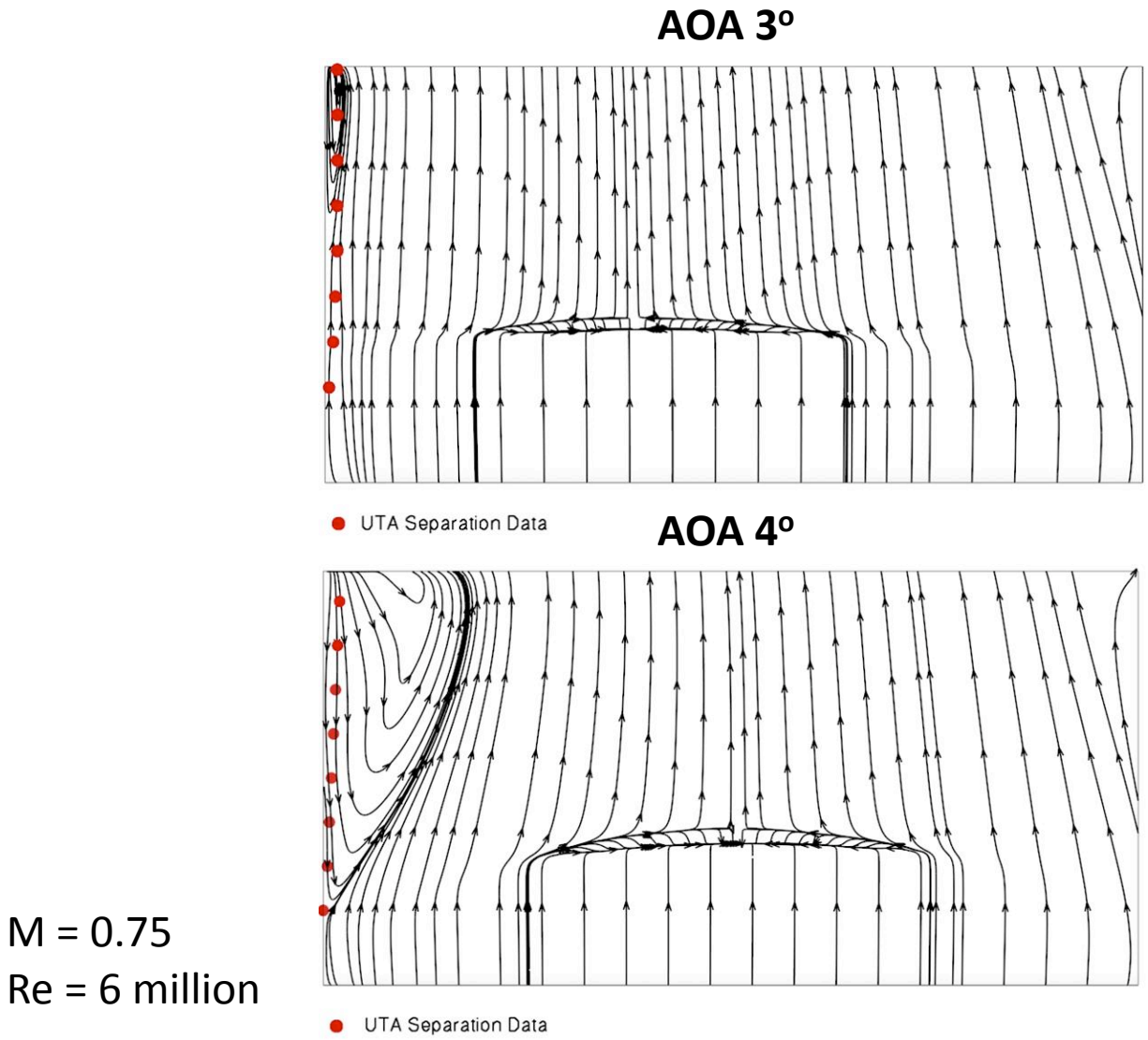
● UTA Separation Data

Figure 6.9: Angles of attack 3° and 4° with streamlines from CFD simulations and data points obtained from experiments at UTA.

but small. The experimental data compares well qualitatively with the simulation. As the angle of attack raises to 4° the shock is pushed outward on the span and becomes less apparent away from the small separation region. The CFD results show the recirculation zone becoming much larger and moving upstream toward the leading edge. The experimental data do not change much. They are no longer qualitatively in good comparison. Quantitatively, the leading edge is very close to the CFD simulation.

6.7 C_p Contour and Streamline Plots

C_p contour and streamline plots were created at selected span locations based on the closest grid lines to reduce interpolation error. The locations were chosen at the middle of the span (0.05122 m from the side wall), in the separation zone for 4° angle of attack (0.00812 m from the side wall), and in the separation zone for 3° angle of attack (0.00112 m from the side wall). These can all be seen in Figure 6.10. Both angles of attack show a shock and little separation in the middle of the span. Separation can be seen behind the shock in Figure 6.11, but it is very slight. Closer to the wall the angle of attack 4° case has a large recirculation zone at the trailing edge. Furthermore, the shock has moved closer to the leading edge and is almost nonexistent for angle of attack 4°. At the cut closest to the wall the circulation zone for angle of attack 4° has increased in size while the recirculation zone for angle of attack 3° case has just become noticeable. The shock for the angle of attack 4° case is nonexistent while the shock for the angle of attack 3° case is greatly reduced.
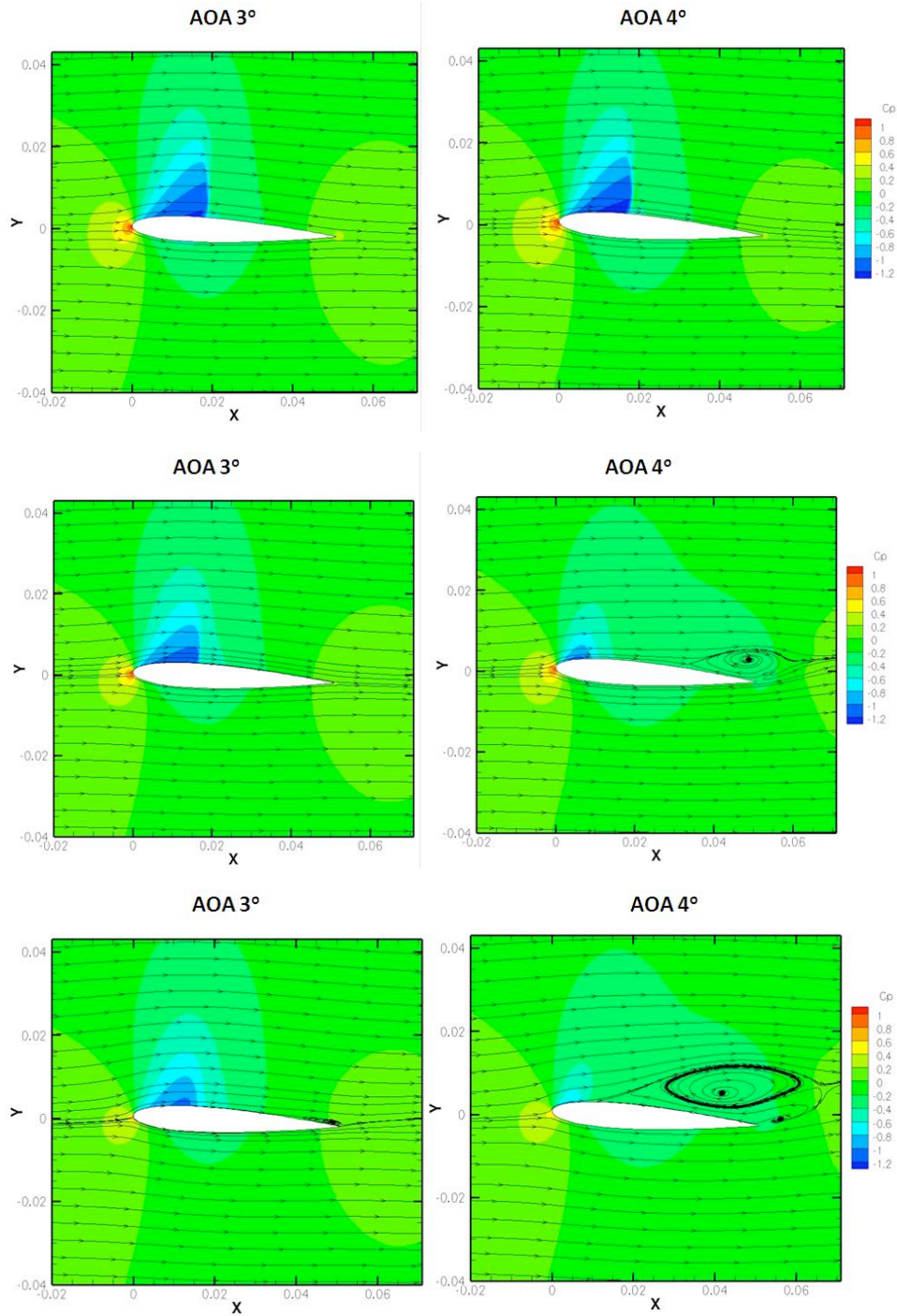
Figure 6.10: C_p contour plots at angles of attack 3° and 4° at M=0.75 and Re = 6 million.

Top: Spanwise location 0.05122 m from the wall. Bottom: Spanwise location 0.00812 m from the wall. Bottom: Spanwise location 0.00112 m from the wall.
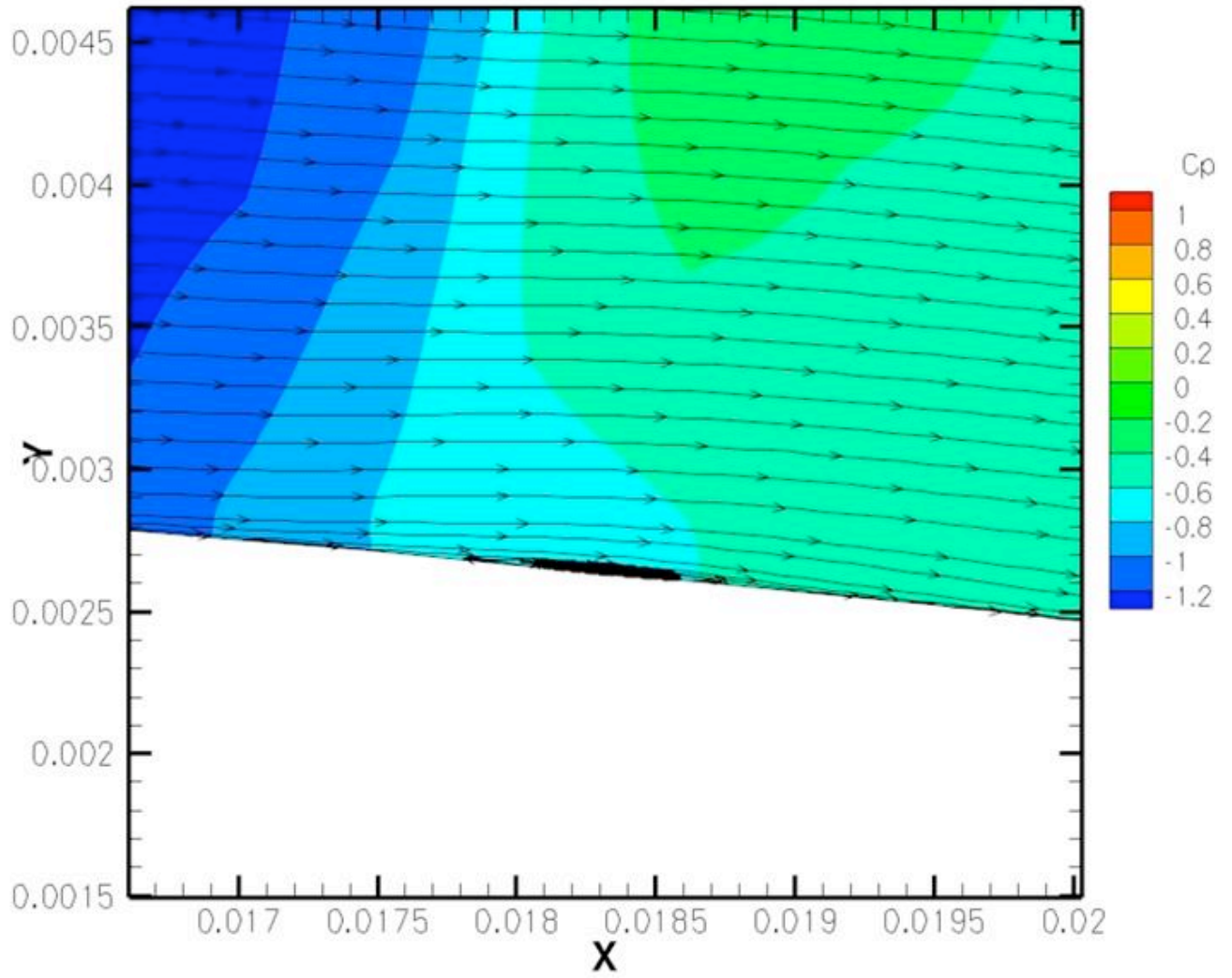
Figure 6.11: Angle of attack 4°: Zoomed view of separation zone.

6.8 Comparison of SRQs to Angle of Attack and Boundary Layer Changes

The changes in angle of attack and boundary layer have an effect on the SRQs. These effects are quantified in Table 6.3. Notice a small change in angle of attack produces a large change in all of the SRQs. This is due to the separation zone in the interaction region increasing in size. The C_D increases dramatically while the distance between the leading edge and the beginning of the separation zone decreases. Both the maximum separation distance and separation at 88.8% chord increase.

The boundary layer growth has a small effect on the SRQs, also seen in 6.4. The boundary layer growth tends to change the freestream Mach number, which has an effect on the SRQs. It also reduces the dynamic pressure felt over some of the NACA 0012's span. The data show that as the boundary layer grows, the C_d decreases slightly and the LE increases slightly. The maximum span and span at 88.8% decrease slightly.

Table 6.3: Comparison of SRQs to Angle of Attack

	SRQs	AOA 3°	AOA 4°
	C_d	0.00375	0.01232
Beginning Boundary Layer	LE (x/c)	0.5529	0.1706
	Max Span (y/b)	0.01703	0.1165
	Span at 88.8% (y/b)	0.01576	0.1162

Table 6.4: Comparison of SRQs to Boundary Layer Changes

	SRQs	Beginning	Ending
	C_d	0.01075	0.01032
Angle of Attack 4°	LE (x/c)	0.1853	0.1913
	Max Span (y/b)	0.1052	0.1039
	Span at 88.8% (y/b)	0.1048	0.1034

6.9   Parametric Study

The parametric study involves numerous simulations to assess the flow at various angles of attack, Mach number, and inlet conditions. This provides a better comparison with experimental data by accounting for some of the known tunnel uncertainties, specifically changes in Mach number and boundary layer growth.

The experimental data is taken at $M = 0.75 \pm 0.02$ and is reported as having a normal distribution by the experimentalists [42]. This distribution can be replicated in the simulation by sampling from the Mach number CDF to create a CDF of the SRQs. The entrance boundary layer is accounted by running the simulation at the starting and ending conditions, resulting in two CDFs. The numerical uncertainty from the grid study is included by subtracting the numerical uncertainty from the lower of the two CDFs and adding the numerical uncertainty to the higher valued CDF. This creates a p-box for each of the SRQs.

The C_D has not been measured experimentally so only the numerical uncertainty could be assessed. The C_D has a relatively moderate numerical uncertainty compared to epistemic
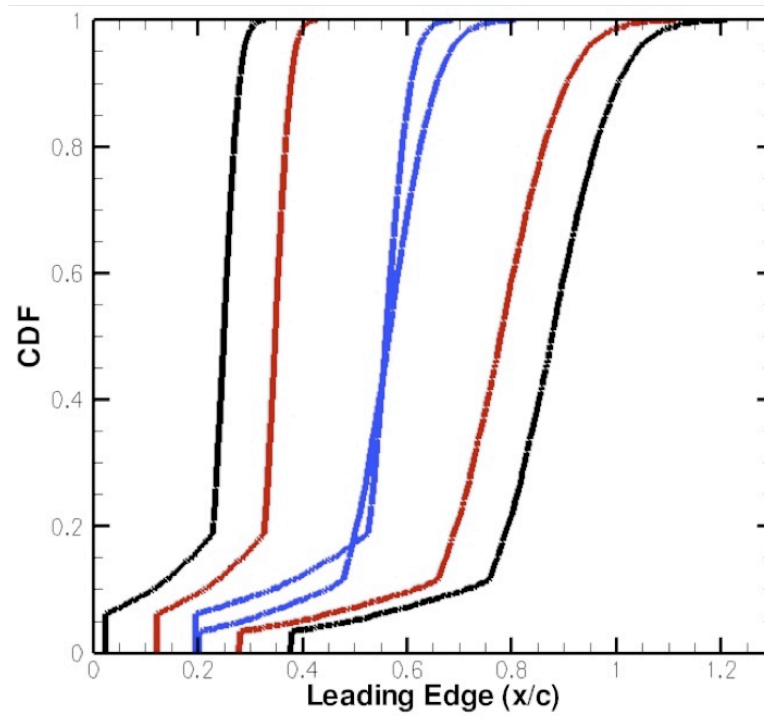
Figure 6.12: Leading edge SRQ p-box for angle of attack 3°.

uncertainty. Figures 6.12 and 6.13 show the LE SRQ agrees poorly with experimental data, though the experimental data is within the relatively large numerical uncertainty. The separation SRQs, Figures 6.14, 6.15, 6.16, 6.17, show good agreement before the separation becomes very large. Angle of attack 3° shows a small model form uncertainty while angle of attack 4° has large model form uncertainty.

6.10   Porous Wall Modeling

An assumption of solid walls was made early in the study. A more intensive study of how porous walls affects SRQs is required. The experimentalists measured Mach number
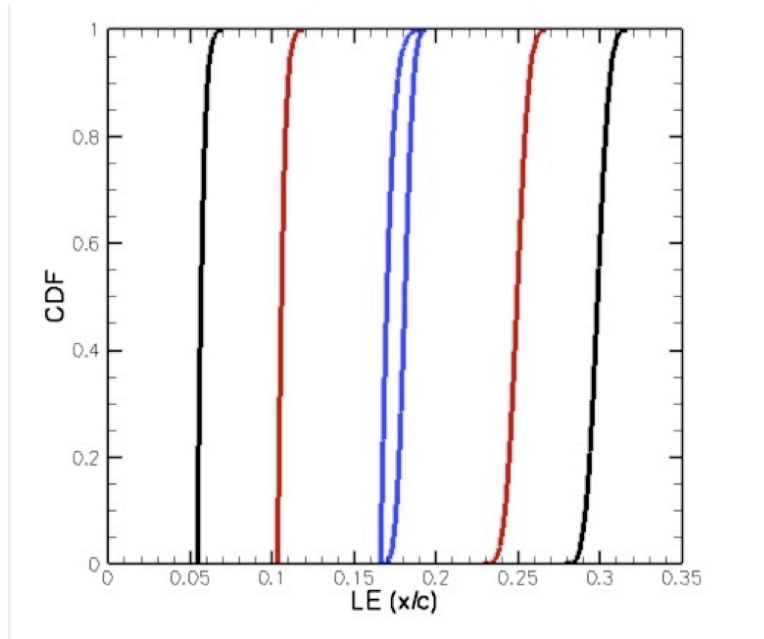
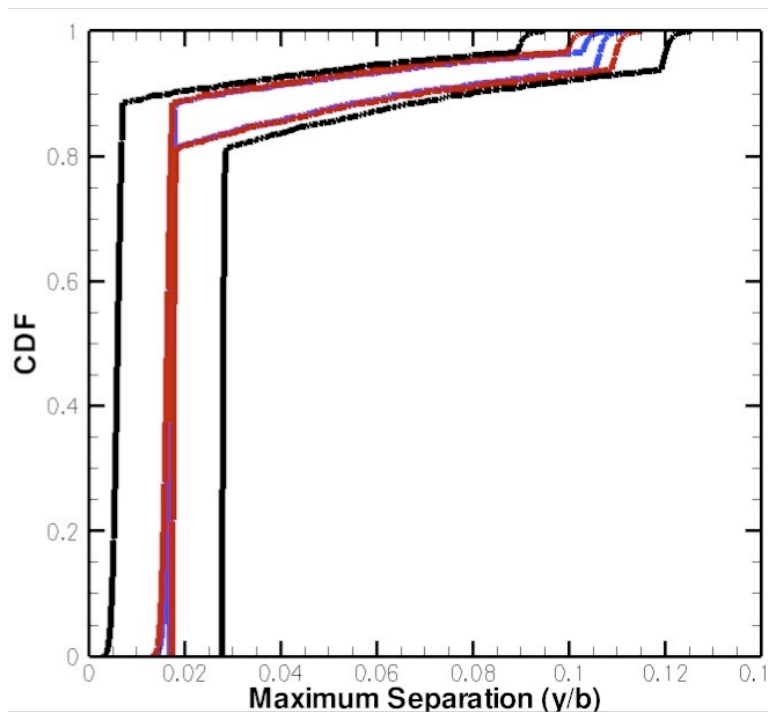Figure 6.13: Leading edge SRQ p-box for angle of attack 3°.

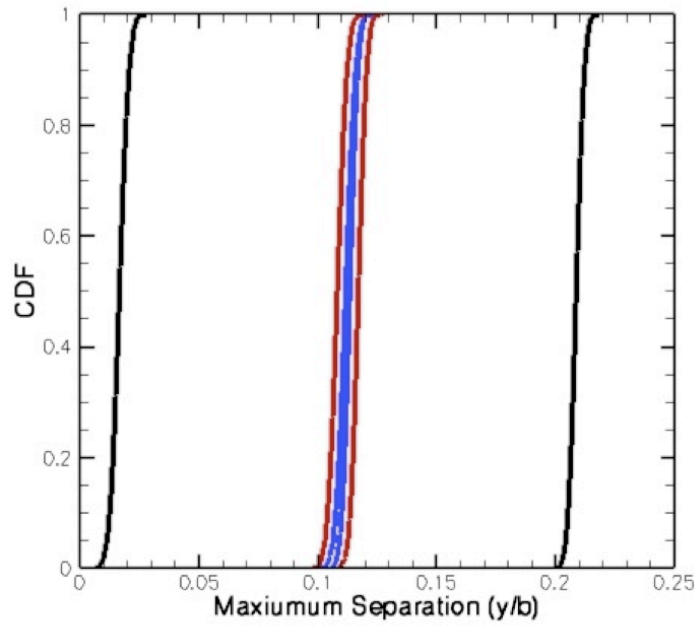Figure 6.14: Maximum separation SRQ p-box for angle of attack 3°.

Figure 6.15: Maximum separation SRQ p-box for angle of attack 4°.

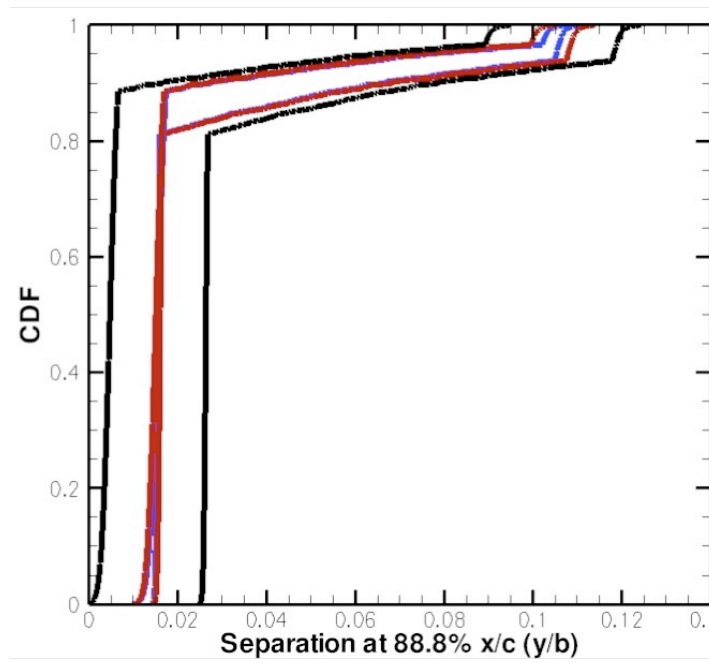
Figure 6.16: Separation at 88.8% SRQ p-box for angle of attack 3°.
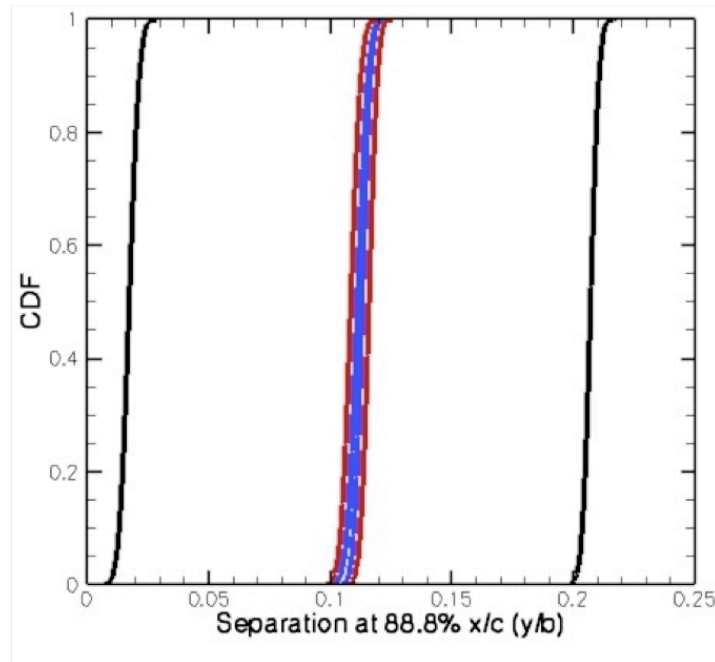
Figure 6.17: Separation at 88.8% SRQ p-box for angle of attack 4°.

at three locations at or near the centerline of the tunnel across from the NACA 0012 fin. These experimental measurements were compared against the computational centerline Mach number results. The comparison between the two was poor. The Mach number in the experiment tended to decrease through the tunnel while the computational Mach number increased through the tunnel. This is expected since the growth of the boundary layer would act to decrease the tunnel area, therefore increasing the Mach number.

The easiest method of changing the centerline Mach number is changing the area through the tunnel. The top and bottom walls remain solid, but are angled out to account for the mass lost due to the porous wall condition. The angling and back pressure is adjusted until the centerline Mach number matches the first experimental measurement. A comparison between the various centerline Mach numbers can be seen in Figure 6.18.
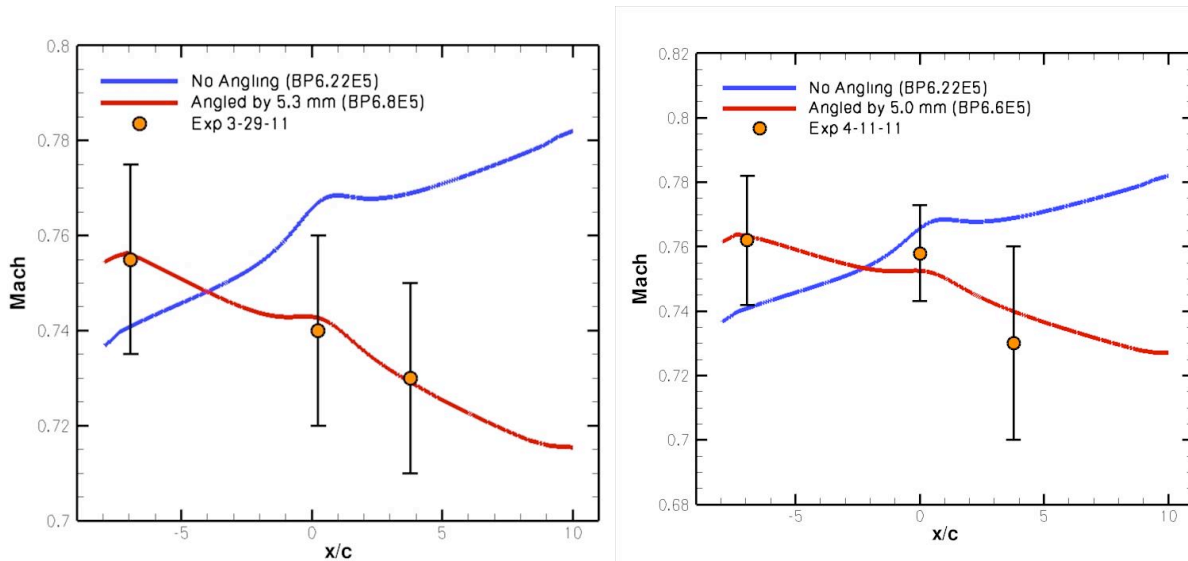
Figure 6.18: Mach centerline measurements of experiment, solid walls, and angled walls. Angle of attack 7° on the left and angle of attack 4° on the right.

The result from this comparison showed very little change in the SRQs. Table 6.5 shows how the leading edge and max separation SRQs change for the angle of attack 4° case. Both SRQs vary by less than 6%, or less than they would vary by a small change in Mach number.

Table 6.5: Comparison of SRQs for Wall Angling for Angles of Attack 4°

SRQs	LE (x/c)	Max Span (y/b)
No Angling	0.1853	0.1424
Angled by 5.0mm	0.1958	0.1342

6.11 Angle of Attack 7° Tests

The experimentalists tested at angle of attack 7° late in the study. As seen in Figure 6.19 the separation zone is visible and large for the experimental case. This figure also shows the CFD prediction, which has larger separation behind the shock. Propagation of the aleatory and epistemic uncertainties was not feasible due to time constraints, but a quick comparison between the two was possible. Table 6.6 shows the changes in the SRQs. Qualitatively, the angle of attack 7° case is much closer to the CFD prediction. Quantitatively, they are still far apart.

Table 6.6: Comparison of SRQs for Wall Angling for Angles of Attack 7°

SRQs	LE (x/c)	Max Span (y/b)
Experiment	0.3750	0.0648
CFD Prediction	0.0989	0.1462
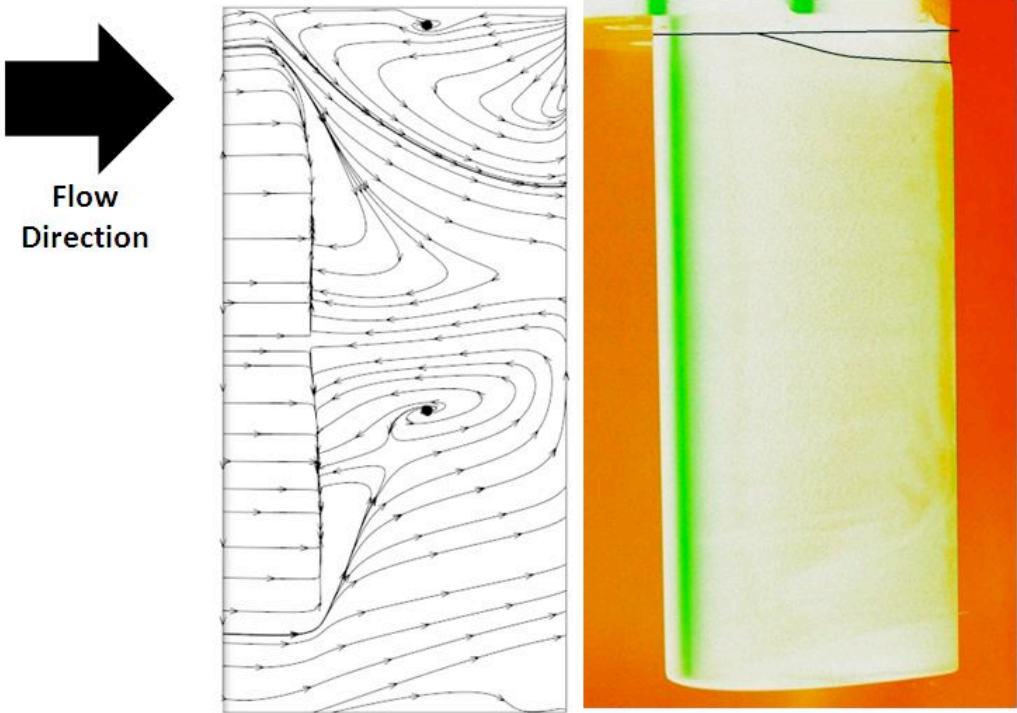
Figure 6.19: Comparison of CFD prediction and oil flow visualization at angle of attack 7°.

Chapter 7

Conclusions

7.1 Results

This study intended to assess turbulence models for high Reynolds number transonic junction flows, specifically, how well the turbulence models predicted separation in these flows. The geometry for the simulations is a wind tunnel with a rectangular cross-section. A NACA 0012 fin was placed in the test section and the angle of attack varied. The nominal test conditions were a Reynolds number of 6 million and a Mach number of 0.75. At low angles of attack (below 3°) there was a small region of separated flow between the side wall and fin. Above 3° angle of attack this separation bubble became very large, stretching across 10% of the span. Also, above 3° the size of the separation bubble does not vary significantly with angle of attack.

This study assessed the known aleatory and epistemic uncertainties present in the experi-

mental test. Experimental Mach number fluctuations were treated as an aleatory uncertainty while the boundary layer growth was treated as an epistemic uncertainty. These two uncertainties were propagated through the model to produce p-boxs for the four SRQs; C_D, separation distance from the leading edge, maximum separation span, and separation span at 88.8% chord. Included in the p-box assessment is the numerical uncertainty, which is mainly composed of discretization uncertainty. The numerical uncertainty compared to the epistemic uncertainty was moderate for C_D, high for the separation distance from the leading edge, and low for both the maximum separation span and the separation at 88.8% chord. The experimental and CFD SRQs did not match and revealed a large model form uncertainty. The cause of the large model form uncertainty was then narrowed to either the porous wall boundary condition or deficiencies in the turbulence model. A study with an approximation of the porous wall boundary condition showed the separation zone was insensitive to this boundary condition.

It can be said with reasonable confidence that the model form error is due to deficiencies in the turbulence model. The specific deficiency in the turbulence model is that it predicts separation being present at lower angles of attack and Mach numbers than is seen in experiment. The assessment of the turbulence model shows decent agreement before major separation. After major separation the turbulence model does not agree well with experimental data. Since the major separation increases the drag, the turbulence model over predicts the interference drag that will occur in transonic flow.

The study also concluded that the Menter 1994 k-ω SST model showed the fastest con-

vergence for this particular case. The Wilcox 1998 k-ω model and Spalart-Allmaras 1992 model showed similar behaviors, but both took longer to converge. The k-ϵ realizable model showed similar behaviors as well, but its convergence behavior was suspect.

7.2 Recommendations for Further Research

7.2.1 CFD

The first suggestion is to use a more calculation intensive turbulence model, such as DES or LES to see if similar separation behaviors are observed. ANSYS Fluent, an unstructured CFD code, was used for this study. Since the grids used in this study are fully structured, it is recommended that a fully structured CFD code be used in future research. While being compatible with the grid, structured solvers are generally regarded as faster solvers since the cells have a clear order.

Since the discretization uncertainty is the second highest known uncertainty, it would be most beneficial to commit resources to reducing it. The grid study shows the observed order of accuracy is not close to the formal order of accuracy. To improve this estimate, at least one more systematically refined grid would be necessary. This grid would likely have to be 8 times larger, or 350 million cells. This would require much more computational resources than are currently available. Another suggestion would be to employ a residual based discretization error estimator, such as the error transport equations. Furthermore, grid adaptation could be used to make each grid more effective with the same number of

cells.

7.2.2   University of Texas at Arlington Tunnel

There are several measurements at the UTA tunnel that would help better characterize the flow, which would reduce tunnel uncertainties. The inflow plane should be measured for boundary layer properties, density, Mach number, temperature, and flow angularity. Also, a careful assessment of the as-built geometry would allow CFD operators to simulate the full tunnel under unsteady conditions.

Chapter 8

Bibliography

Bibliography

[1] Gundlach, J. and et al., "Conceptual Design Studies of a Strut-Braced Wing Transonic Transport," *Journal of Aircraft*, Vol. 37, 2000, pp. 976–983.

[2] Gern, F. H. and et al., "Multidisciplinary Design Optimization of Transonic Commercial Transport with Strut-Braced Wing," *Journal of Aircraft*, Vol. 38, Dec 2001, pp. 154–163.

[3] Boeing, ""787 Dreamliner"," June 2010, http://www.boeing.com/commercial/787family/.

[4] Boeing, "Boeing 787 Factsheet," Jan. 2011, http://www.aerospaceweb.org/aircraft/jetliner/b787/.

[5] Escalona, E., "Airplane 3 View Drawings," Website, January 2011, http://www.fortunecity.com/marina/manatee/272/.

[6] Harris, T., "2010 Challenge: Environmentally Responsible (Green) Aviation College Student Challenge," NASA, August 2010.

[7] "Advanced Concept Studies for Subsonic and Supersonic Commercial Transports Entering Service in the 2030-35 Period," NASA, November 2007.

[8] Pfenninger, W., "Design Considerations of Large Subsonic Long Range Transport Airplanes with Low Drag Boundary Layer Suction," Northrop Aircraft, Inc., Report NAI-54-900 (BLC-76), November 1954.

[9] Seber, G., "Cantilever vs TBW Configuration," October 2010, Private Correspondence.

[10] Tetrault, P., Schetz, J. A., and Grossman, B., "Numerical Prediction of the Interference Drag of a Streamlined Strut Intersection a Surface in Transonic Flow," *AIAA*, 2000.

[11] Duggirala, R., Roy, C., and Schetz, J., "Analysis of Interference Drag for Strut-Strut Interaction in Transonic Flow," *AIAA*, 2009.

[12] Oberkampf, W. L. and Roy, C. J., *Verification and Validation of Scientific Computing*, Cambridge University Press, Cambridge, 2010.

[13] Becker, J. V., *The High-Speed Frontier*, NASA, 1980.

[14] Baals, D. and Stokes, G., "A Facility Concept for High Reynolds Number Testing at Transonic Speeds," *AGARD*, No. 83, NASA Langley, AGARD, 1971, p. 28.

[15] Schetz, J. A., *Boundary Layer Analysis*, Prentice Hall, 1993.

[16] Hoerner, S., *Fluid Dynamic Drag*, Hoerner, 1965.

[17] Chandrasekaran, B., "Computation and Comparison of of the Installation Effect of Compression Pylons for a High Wing Transport," Vigyan Research Associates, Inc., Hampton, VA, AIAA, January 1988.

[18] Naik, D. A., "Innovative Pylon Concepts for Engine-Airframe Integration for Transonic Transports," AIAA, 1989.

[19] Naik, D. A., Ingraldi, A. M., and Pendergraft, O. C., "Experimental Study of Pylon Cross Sections for a Subsonic Transport Airplane," *Journal of Aircraft*, Vol. 30, No. 5, Oct 1993, pp. 676–681.

[20] ANSYS, I., *ANSYS FLUENT 12.0 User's Guide*, ANSYS, Inc, 2009.

[21] Anderson, J., *Computational Fluid Dynamics: The Basics with Applications*, McGraw Hill, 1995.

[22] Ludwieg, H., "Tube Wind Tunnel, a Special Type of Blowdown Wind Tunnel," Tech. Rep. 143, AGARD, 1957.

[23] Vassberg, J. C. and et al., "Comparison of NTF Experimental Data with CFD Predictions from the Third AIAA CFD Drag Prediction Workshop," No. AIAA 2008-6918, 2008.

[24] Ladson, C. L., Hill, A. S., and William G. Johnson, J., "Pressure Distributions from High Reynolds Number Transonic Tests of an NACA 0012 Airfoil in the Langley 0.3-Meter Transonic Cryogenic Tunnel," *NASA*, Dec 1987, NASA TM 100526.

[25] Ladson, C. L. and Ray, E. J., "Evolution, Calibration, and Operational Characteristics of the Two-Dimensional Test Section of the Langley 0.3-Meter Transonic Cryogenic Tunnel," *NASA Scientific and Technical Information Office*, 1987, NASA TP 2749.

[26] Harris, C. D., "Two-Dimensional Arodynamic Characteristics of the NACA 0012 Airfoil in the Langley 8-Foot Transonic Pressure Tunnel," *NASA Technical Memorandum 81927*, April 1981.

[27] Ladson, C. L. and Ray, E. J., "Status of Advanced Airfoil Tests in the Langley 0.3-meter Transonic Cryogenic Tunnel," NASA, 1981, pp. 37–53.

[28] Johnson, W. G. and Hill, A. S., "Pressure Distributions From High Reynolds Number Tests of a Boeing BAC I Airfoil in the Langley 0.3-Meter Transonic Cryogenic Tunnel," Tech. rep., 1985, NASA-TM-100526.

[29] Chu, J., Flechner, S. G., and Hill, A. S., "High Reynolds Number Test of the Boeing TR77 AIrfoil in the Langley 0.3-Meter Transonic Cryogenic Tunnels," Tech. rep., NASA, 1990, NASA-TM-4189.

[30] Murthy, A. V., Johnson, C. B., Ray, E. J., Lawing, P. L., and Thibodeaux, J. J., "Studies of Sidewall Boundary Layer in the Langley 0.3-Meter Transonic Cryogenic Tunnel With and Without Suction," *NASA Technical Paper 2096*, 1983.

[31] Gumbert, C. R. and Newman, P. A., "Validation of a Wall Interference Assessment/Correction Procedure for Airfoil Tests in the Langley 0.3-m Transonic Cryogenic Tunnel," *AIAA-85-2151*, Aug 1984.

[32] Chung, I., Lee, D., and Reu, T., "Prediction of Transonic Buffet Onset for an Airfoil with Shock Induced Separation Bubble using Steady Navier-Stokes Solver," *AIAA*, June 2002.

[33] Wilcox, D. C., *Turbulence Modeling for CFD*, DCW Industries, Inc., 1994.

[34] Wilcox, D. C., "Supersonic Compression-Corner Applications of a Multiscale Model for Turbulent Flows," *AIAA Journal*, Vol. 28, 1990, pp. 1194–1198.

[35] Menter, F. R., "Two-Equation Eddy-Viscosity Turbulence Models for Engineering Applications," *AIAA Journal*, Vol. 32, 1994, pp. 1598–1605.

[36] Clarke, D. J. D., "Simulation of a Wing-Body Junction Experiment using the Fluent Code," DSTO-TR-1731, June 2005.

[37] Spalart, P. and Allmaras, S. R., "A One-Equation Turbulence Model for Aerodynamic Flows," *AIAA*, 1992.

[38] Tetrault, P.-A., *Numerical Prediction of the Interference Drag of a Streamlined Strut Intersecting a Surface in Transonic Flow*, Master's thesis, Virginia Tech, 2000.

[39] Bartelheimer, W., Horstman, K. H., and Puffert-Meissner, W., "2-D Airfoil Tests Including Side Wall Boundary Layer Measurements," *A Selection of Experimental Test Cases for the Validation of CFD Codes*, 1994.

[40] Starr, R., "Experiments to Assess the Influence of Changes in the Tunnel Wall Boundary Layer on Transonic Wall Crossflow Characteristics," TR-75-97, 1975.

[41] Braun, E., January 2011, Private Correspondence.

[42] Braun, E., "Side Wall Arrangement," March 2010, Private Correspondence.

[43] Starr, R., "Experimental Studies of a Ludwieg Tube High Reynolds Number Transonic Tunnel," TR-73-168, 1973.

[44] Rumsey, C., "Turbulence Modeling Resource," June 2010, http://turbmodels.larc.nasa.gov/.

[45] Hirsch, C., *Numerical Computation of Internal and External Flows*, Vol. 2, Wiley, 1984.

[46] Pointwise, *Gridgen*, Pointwise, Fort Worth, Texas.

[47] Hatton, "The T-Experiments: Errors in Scientific Software," April 1997.

[48] Phillips, T. and Roy, C., "Evaluation of Extrapoltion-Based Discretization Error and Uncertainty Estimators," No. AIAA Paper 2011-215, 2011.

[49] Richardson, L. F., "The Approximate Arithmetical Solution by Finite Differences of Physical Problems involving Differential Equations, with an Application to the Stresses in a Masonry Dam." *The Royal Society*, 1911, pp. 307–357.